

**PARAGLACIAL LANDSCAPE EVOLUTION IN A RAPIDLY
DEGLACIATING ENVIRONMENT**

A Case Study of Taan Fjord, Southeast Alaska, USA

by

Haley Williams

B.Sc., Alaska Pacific University, 2014

A THESIS SUBMITTED IN PARTIAL FULFILLMENT OF
THE REQUIREMENTS FOR THE DEGREE OF

MASTER OF SCIENCE

in

THE FACULTY OF GRADUATE AND POSTDOCTORAL STUDIES
(Geography)

THE UNIVERSITY OF BRITISH COLUMBIA
(Vancouver)

August 2018

© Haley Williams 2018

The following individuals certify that they have read, and recommend to the Faculty of Graduate and Postdoctoral Studies for acceptance, a thesis/dissertation entitled:

“Paraglacial landscape evolution in a rapidly deglaciating environment: A case study of Taan Fjord, Southeast Alaska, USA”

submitted by **Haley Williams** in partial fulfillment of the requirements for

the degree of **Master of Science**

in **Geography**

Examining Committee:

Michele Koppes

Supervisor

Brett Eaton

Supervisory Committee Member

Marwan Hassan

Additional Examiner

Abstract

The rapid thinning and retreat of Tyndall Glacier in Taan Fjord in Southeast Alaska has exposed 8 fluvial tributary watersheds to fast-acting paraglacial denudation processes. An average base-level fall of ~ 400 m has resulted in increased sediment yields and basin-averaged erosion rates in the watersheds over the first decades following the exposure of their outlets to the ocean. We used structure from motion photogrammetry to reconstruct the rate of surface thinning of Tyndall Glacier since 1957 and the rate of base-level fall for the tributaries. We modelled each fan-delta to obtain a minimum estimate of total sediment volume evacuated from each watershed and used geometric relations to determine sediment yields and erosion rates for each tributary through time. Between 1969 and 2014, the tributary basins contributed 165.7 ± 16.0 million m^3 of total sediment to the fjord, or double the amount of sediment contributed by Tyndall Glacier. On average, the tributaries eroded their watersheds at a rate of 36.0 ± 5.7 mm yr^{-1} and yielded three times more sediment annually than the glacier at 4.3 ± 0.3 million $\text{m}^3 \text{yr}^{-1}$. Base-level fall led to knickpoint formation in most watersheds with an average rate of migration exceeding 20 m yr^{-1} . Those tributaries that have had the most time to respond to base-level fall have passed their peak sediment yields that are expected during the paraglacial period and have experienced the greatest landscape relaxation since the retreat of Tyndall Glacier. In contrast, the tributaries that have experienced base-level fall most recently at the head of the fjord are eroding their watersheds at a rapid pace, indicating that they are in the throes of the highly dynamic paraglacial period. In addition to the small-magnitude unravelling of the tributary basins, a large tsunamigenic landslide occurred in the fjord in 2015. This event as well as the high sediment yields observed

in the tributary basins highlight the potential hazards associated with paraglacial landscapes. These rapidly changing environments are becoming more important to study in order to understand the changes that might occur in glaciated regions as climate continues to warm and glaciers continue to retreat.

Lay Summary

Between 1961 and 1999, Tyndall Glacier in Taan Fjord in Southeast Alaska retreated extremely rapidly and exposed new areas of land to fast-acting processes that have dramatically changed the face of Taan Fjord. Tributary streams adjusted to the loss of the glacier by cutting down through loose sediment and bedrock. Additionally, a massive landslide occurred in the fjord in 2015 that created a tsunami 192 m high. This large-magnitude event as well as the small-magnitude unravelling processes happening in the tributaries of Taan Fjord are known as “paraglacial” processes. In this study, we demonstrate how effective these paraglacial processes can be in changing entire landscapes. This information can be used to anticipate future trends likely to be seen in glaciated regions around the world as climate continues to warm. The better we understand these paraglacial processes, the better prepared we’ll be for an era of continued glacier retreat.

Preface

The research topic and study design was developed by Haley Williams, Michele Koppes, and Brett Eaton. Structure from motion digital terrain models were created and analyzed by Haley Williams with guidance from Brett Eaton. The volumetric models used in this analysis were informed by Brett Eaton and implemented by Haley Williams. Determination of sediment yields and erosion rates as well as interpretation of the results were performed by Haley Williams and guided by feedback from Michele Koppes. The manuscript was prepared by Haley Williams with editing by Michele Koppes and Brett Eaton.

Table of Contents

Abstract	iii
Lay Summary	v
Preface	vi
Table of Contents	vii
List of Tables	ix
List of Figures	x
List of Symbols	xii
List of Abbreviations	xiii
Glossary	xiv
Acknowledgements	xvi
Chapter 1: Introduction	1
1.1 Background	1
1.2 Paraglacial Hazards	3
1.3 Research Gaps and Motivation	5
1.4 Study Location	6
1.4.1 Glacial History	7
1.4.2 Geology	8
1.4.3 October 2015 Landslide	10
1.5 Study Goals	11
1.6 Thesis Structure	12
Chapter 2: Methods	13
2.1 Glacier Thinning and Retreat	14

2.2 Watershed Delineation and SfM	15
2.3 Volume Models	18
2.3.2 Geometry	19
2.3.2.1 Fan-Delta Model 1.....	20
2.3.2.2 Fan-Delta Model 2.....	23
2.3.2.3 Fan-Delta Model 3.....	24
2.3.3 Error Analysis	25
2.4 Sediment Yields and Erosion Rates	27
Chapter 3: Results	30
3.1 Thinning Rates	30
3.2 Tributary Watersheds	34
3.2.1 Watershed Characteristics	34
3.2.2 Morphological Evolution	36
3.2.3 Error in Volume Models	39
3.2.4 Sediment Yield and Basin-Averaged Erosion Rates.....	42
Chapter 4: Discussion	50
4.1 Geomorphic Evolution	50
4.1.1 Geomorphic Evolution: Watershed 1967	53
4.2 Sediment Yields and Erosion Rates	54
4.2.1 Lithology and Bedrock Structure	56
4.2.2 Variables Driving Change	58
4.2.3 Assumptions	59
4.4 October 2015 Landslide & Tsunami	60
4.4.1 Fan-Delta 1988	62
4.5 Tyndall Glacier, Taan Tributaries, and the 2015 Landslide	63
4.6 Future Paraglacial Relaxation of Taan Fjord	67
4.6.1 Timeline of Relaxation	69

Chapter 5: Conclusions	71
5.1 General Conclusions	72
References.....	75
Appendix I.: Structure from Motion Photogrammetry	80
A.1 Background.....	80
A.2 Workflow	80
A.3 Error Quantification.....	84

List of Tables

Table 2-1. Imagery used for glacier and tributary basin analyses.	15
Table 2-2. Model parameters needed to obtain volumes for the fan-deltas of Taan Fjord.	19
Table 2-3. Maximum and minimum values used for model parameters	27
Table 2-4. Surface area ratios and area to volume ratios that were used for each fan-delta to obtain volumes in years that lacked enough data to be used in the model for volume calculation.	28
Table 3-1. Total base level fall and average rate of fall for all tributaries	33
Table 3-2. Fan-delta, stream, and watershed characteristics as well as general geologic setting for each tributary basin.	35
Table 3-3. Tabulated results for total fan-delta volume, sediment yield, and basin averaged erosion rate including minimum and maximum yields and erosion rates	44
Table A-1. Photoscan processing parameters.....	81
Table A-2. Mean error and standard deviation of error distributions for each model	83

List of Figures

Figure 1-1. Relative sediment yield rates displayed as a comparison between small and major valleys	3
Figure 1-2. Icy Bay and Taan Fjord in Southeast Alaska	7
Figure 1-3. Tyndall glacier termini positions.....	8
Figure 1-4. Fault systems around Icy Bay, the Malaspina Glacier and Bagley Icefield.....	9
Figure 2-1. Tributary watersheds and fan-deltas of Taan Fjord	17
Figure 2-2. Fan-delta geometries across the three different models	20
Figure 2-3. Detailed depiction of variables involved in volume model 1.....	22
Figure 2-4. Flowchart of methods used to obtain fan-delta volumes.....	28
Figure 3-1. Centerline elevation of Tyndall Glacier from 1957 – 2016	31
Figure 3-2. Cross sections across the fjord at the location of each tributary outlet from 1957 – 2016.....	32
Figure 3-3. Total base level fall at the outlet of each tributary watershed since 1957.	34
Figure 3-4. The outlet of watershed 1967 in the years 1957, 1969, 1974, and 2013.....	37
Figure 3-5. Longitudinal profiles for each stream	39
Figure 3-6. Monte Carlo volume distributions for each fan-delta in Taan Fjord.....	41
Figure 3-7. Total volume in the fan-deltas of Taan Fjord in 2014 (pre-tsunami).....	42
Figure 3-8. Volume growth of each fan-delta since fan-delta progradation began	45
Figure 3-9. Average sediment yields (a) and basin-averaged erosion rates (b) for all tributary basins on a logarithmic scale.	47
Figure 3-10. Basin-averaged erosion rates and sediment yields of the eight tributary basins	48

Figure 3-11. Basin-averaged erosion rates and sediment yields of the eight tributary basins of Taan Fjord plotted together at the same scale.....	49
Figure 4-1. FD 1967 between 1974 and 1976 in which it experienced rapid growth.....	54
Figure 4-2. Watershed 1983 in 1957 (left) and 2014 (right).....	55
Figure 4-3. Map detailing the geologic units and active faulting in Taan Fjord.....	58
Figure 4-4. Graphs comparing the sediment output from the tributary watersheds to the sediment output of the glacier and the instantaneous output from the October 2015 landslide.....	64
Figure A-1. Workflow of PhotoScan steps beginning with aerial photos and ending with a DTM.	79
Figure A-2. The four models with associated error polygons.....	83

List of Symbols

- \pm Denotes positive and negative error around an estimate
- Σ Denotes the summation of terms that follow in an equation
- β Foreset bed angle of the fan-deltas (radians)
- θ Splay angle of the fan apex (radians)
- ρ Density (km m^{-3})

List of Abbreviations

a.s.l.	above sea level
b.s.l.	below sea level
DEM	Digital Elevation Model
DTM	Digital Terrain Model
IfSAR	Interferometric Synthetic Aperture Radar
LGM	Last Glacial Maximum
LiDAR	Light Detection and Ranging
MC	Monte Carlo
MHHW	Mean Higher High Water
PDF	Probability Density Function
SfM	Structure from Motion
UAF	University of Alaska Fairbanks
USGS	United States Geological Survey

Glossary

Accumulation zone: Region of a glacier where it gains mass in the form of snow.

Alluvial fan: Fan-shaped deposit of river-sourced sediment.

Alluvium: Sediment deposited by rivers.

Angle of repose: Steepest angle at which sediment can accumulate and still maintain stability.

Arkosic: Describes sedimentary bedrock rich in feldspar.

Base-level: Elevation at the outlet of a river.

Braided: Type of river morphology with a network of many channels separated by bars.

Bulk density: Total density of sediments, pore spaces, and water.

Calving: Process by which ice is lost at the terminus of a tidewater glacier.

Colluvium: Sediment deposited due to gravity (i.e. rockfall).

Convergence: Process of tectonic plates moving towards one another.

Delta toe: Maximum extent or edge of the subaqueous delta.

Fan apex: The point at which deposition begins on the fan-delta.

Fan-delta: “prism of sediments delivered by an alluvial fan and deposited, mainly or entirely subaqueously, at the interface between the active fan and a standing body of water” (Nemec and Steele, 1988).

Glacial debuitressing: Loss of the normal force applied by the weight of glacier ice.

Glacigenic: Sourced from a glacier.

Glacimarine: Glacial sediment deposited in the ocean.

Glaciofluvial: Glacial sediment reworked and deposited by rivers.

Glaciolacustrine: Glacial sediment deposited in a lake.

Knickpoint: Point along a river profile where there is a marked change in channel slope.

Lithology: The physical characteristics of rocks.

Mean higher high water: A tidal datum that uses the average of the two highest tide levels in a daily tidal cycle.

Moraine: A deposit of unconsolidated glacial till.

Morphology: The particular physical form of something (i.e. rivers).

Outwash: Glacial sediment reworked and deposited by glacial meltwater.

Paraglacial: Processes, landforms, and landscapes that are conditioned by glaciation or former glaciation.

Proglacial: Term describing area in front of or at the terminus of a glacier.

Prograde: Outward accumulation of sediment on a delta into a water body.

Sediment yield: The total volume of sediment evacuated from a basin in a fixed amount of time.

Single-thread: Type of river morphology defined by one single channel.

Subaerial: Above the surface of the water.

Subaqueous: Below the surface of the water.

Subglacial: Below a glacier at its base.

Tidewater glacier: A glacier which terminates in the ocean or a lake.

Till: Unconsolidated glacial sediment.

Tsunamigenic: Adjective describing a process by which a tsunami is generated.

Acknowledgements

I thank Michele Koppes for not only being a strong role model for me as a woman in the geosciences, but also for helping me craft my research questions and think critically about how my results translate to a better understanding of the natural world.

I owe special thanks to Brett Eaton for recognizing the need to bring me back to the right path and helping in every way possible to help me achieve my goals.

I express deep gratitude to those faculty and staff at UBC who have helped facilitate my deeper understanding of and passion for the geosciences. Special thanks to my peers in the Geography Department for offering their unwavering support and valuable feedback.

Chapter 1: Introduction

1.1 Background

Between 1983 and 2012, average global temperature has risen $0.85 \pm 0.2^{\circ}\text{C}$ and future projections anticipate further warming, regardless of actions to mitigate CO_2 emissions (Pachauri et al., 2014). The rise in global temperature has spurred climatic changes all across the Earth. Glaciers are particularly sensitive to changes in climate, and an increase in atmospheric temperature has resulted in significant global ice shrinkage since 1961 (Berthier et al., 2010; Pachauri et al., 2014). As global temperatures continue to rise, almost all glaciers will continue to retreat (Marzeion et al., 2014; Pachauri et al., 2014; Radić and Hock, 2011; Radić et al., 2013). This rapid ice loss has exposed and will continue to expose vast landscapes that were previously locked into glacially dominated environments. The sudden shift in regime from glacial to “paraglacial” (those processes, landforms and sediments conditioned by former glaciation and deglaciation) has resulted in rapid responses of landscapes in their pursuit of a new, ice-free equilibrium (Ballantyne, 2002; Church and Ryder, 1972; Lane and Bakker, 2017). These responses can be sudden and catastrophic, such as the triggering of a landslide due to changes in internal stresses of bedrock and debuttressing of valley walls as ice thins and retreats. Relaxation of a landscape after deglaciation can also be slow enough to persist for decades to centuries depending on the scale of the system (Ballantyne, 2002; Church and Slaymaker, 1989; Slaymaker, 2009).

Paraglacial landscapes are considered to be “conditioned” by glaciation because the behaviors of retreating glaciers establish the foundation of future geomorphic change in a landscape. The magnitude of this future change is driven primarily by four conditions left in the wake of retreating glaciers including, (1) the total volume and size of unconsolidated glacial

sediments left behind, (2) the degree of debuttressing of valley walls, (3) the resulting base-level fall in tributary basins stemming from the thinning of ice, and (4) the degree of connectivity in a landscape between the headwaters and the outlet (Lane and Bakker, 2017). In addition to initially heightened sediment output from retreating glaciers themselves (Hallet et al., 1996; Koppes et al., 2010; Koppes and Hallet, 2002; Leonard, 1997), the first three conditions contribute to overall sediment availability in a paraglacial landscape. However, the sediment yield of a paraglacial landscape will be constrained by how efficiently the sediment can cascade through the system, (i.e. it's connectivity). Additional variables can influence the pace of geomorphic change in a paraglacial landscape including regional tectonic movement, bedrock lithology, and climate (Ballantyne, 2002; Schumm, 1993).

In general, sediment yields during and following deglaciation are significantly higher in paraglacial landscapes than yields from non-paraglacial denudation of a landscape (Ballantyne, 2002; Church and Ryder, 1972; Hallet et al., 1996; Ryder, 1971). Sediment yields can be so high that sediment cannot be effectively transported by fluvial systems and are instead stored (Church and Ryder, 1972; Lane and Bakker, 2017). During and immediately following glacier retreat, paraglacial sediment accumulates in proglacial areas where large till-sourced clasts cannot be transported by proglacial rivers, in headwaters where hillslope generated debris is too large to be entrained, or in large paraglacial fans (Lane and Bakker, 2017; Ryder, 1971).

Sediment yields tend to decrease as the paraglacial period progresses, but intermittent pulses of sediment from incising rivers or debris flows can temporarily increase sediment yield (Ballantyne, 2002; Jaegar and Koppes, 2015; Lane and Bakker, 2017). These sources can come from those aforementioned areas of the landscape where paraglacial sediment is stored as a result of transport inefficiency following deglaciation. Additionally, the frequency of major rock mass

movements (landslide and rockfall events) are high during the initial stages of deglaciation and subsequently decrease with time (Arsenault and Meigs, 2005; Ballantyne, 2002; McColl, 2012), thereby boosting sediment yields in the early paraglacial period. Thus, a landscape is deemed “paraglacial” until unstable and metastable glacial deposits reach stability or are exhausted (Ballantyne, 2002). The paraglacial period is therefore scale-dependent and can persist between timescales of 10^1 years for small basins to 10^4 years or even longer for the largest valleys, as illustrated in figure 1-1 (Ballantyne, 2002; Slaymaker, 2009).

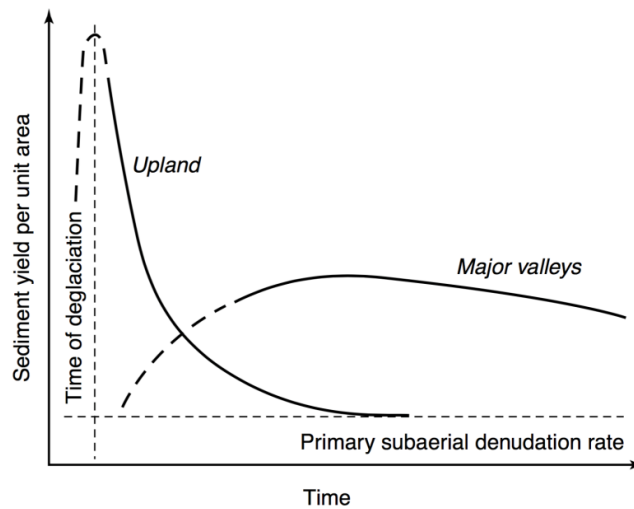


Figure 1-1. Relative sediment yield rates displayed as a comparison between small and major valleys (Ballantyne 2002; Church and Slaymaker, 1989).

1.2 Paraglacial Hazards

Increased sediment yields in fluvial systems during deglaciation can have a variety of negative effects on downstream environments. Larger sediment loads in rivers can have potentially damaging effects on water quality and aquatic habitat (Huss et al., 2017). Any changes in the volume and size of sediment can also change the morphology of rivers (Church, 2015). These changes can lead to an increase in the size and frequency of flooding events (Curran et al., 2017; Huss et al., 2017). Infrastructure downstream of retreating glaciers is potentially the most at-risk in paraglacial environments, particularly hydropower infrastructure

(Huss et al., 2017; Schaepli et al., 2007). Specifically, high sediment inputs can lead to infilling of reservoirs and damage to hydroelectric turbines through abrasion (Huss et al., 2017; Schaepli et al., 2007).

Along with high sediment yields and their effects on fluvial systems, the frequency of major rock mass movements on hillslopes (landslides and rockfall events) are elevated during the early paraglacial period (Arsenault and Meigs, 2005; Ballantyne, 2002; McColl, 2012).

Populations downstream of retreating glaciers may face life-threatening risks as a result of these large mass wasting events (Bornhold et al., 2010; Hewitt, 1998; Lastras et al., 2007). Direct impacts from a landslide or rockfall could destroy entire villages or access roads (Hewitt, 1998; Huggel, 2009). They could also create secondary events, such as large tsunamis or glacier lake outburst floods (Bornhold et al., 2010; Dufresne et al., 2018; Lastras et al., 2007; Wiczorek et al., 2007).

These potential consequences of rapid paraglacial landscape evolution immediately following glacier retreat aren't well quantified simply because humanity has never faced such a drastic drawdown in ice volume and extent in such a short amount of time. No direct observations exist of the immediate processes that occurred in landscapes during the last large ice drawdown following the Last Glacial Maximum (LGM). This lack of direct observations means our understanding of the last major period of deglaciation in Earth's history is limited to interpretations of landforms left behind during this time. While climate change is resulting in the global shrinkage of glaciers, it's also providing a unique opportunity to study and document paraglacial relaxation processes as they happen in real time.

1.3 Research Gaps and Motivation

Previous studies of paraglacial processes have tended to focus on the long-term effects of glaciation on landscapes (Church and Ryder, 1972; Church and Slaymaker, 1989). Typically, theories about the paraglacial period and paraglacial processes were developed by interpreting paraglacial landforms deposited following the LGM ~10kyr ago. The theories are therefore susceptible to interpretation error due to lack of real-time observations (Church and Ryder, 1972; Ryder, 1971). There are few studies that document the evolution of a paraglacial landscape in its entirety from the onset of deglaciation to the modern-day. This is mainly because it is rare to find a landscape to study in which its evolution has been documented thoroughly for several decades following the onset of deglaciation. Additionally, the interplay between retreating glaciers and the new landscapes exposed as a result of their retreat hasn't been explored in much detail. With increased awareness of the effects of climate change on glaciers worldwide after the turn of the 21st century, paraglacial landscapes are becoming more of a focus for researchers seeking to understand the processes and events that are likely to happen directly following glacier retreat worldwide (Ballantyne, 2002; Ballantyne and Stone, 2013; Fischer et al., 2012; Huggel, 2009; Knight and Harrison, 2014; McColl, 2012; Slaymaker, 2011).

The fact that almost all glaciers are in phases of retreat globally in addition to the considerable amount of imagery available today provide a unique opportunity to witness landscape evolution following deglaciation in real-time. Quantifying the magnitude and timing of relaxation of modern-day landscapes during deglaciation has the potential to aid in the understanding of the changes that are likely to occur in glaciated regions as temperatures continue to rise. Any information gained will become invaluable data for communities and populations that are at particular risk of the effects of processes that can be attributed to

deglaciation. This research aims to quantify and document the evolution of a paraglacial landscape that has recently experienced rapid deglaciation in the hopes of shedding more light on what to expect of the world's glaciated regions as climate continues to warm.

1.4 Study Location

Taan Fjord is located in Icy Bay ~100 km northwest of the nearest village of Yakutat in the St. Elias orogen in Southeast Alaska, USA (figure 1-2). The fjord emerged in 1960 when Tyndall Glacier separated from the main trunk glacier in Icy Bay (Koppes and Hallet, 2006; Meigs et al., 2006). Tyndall Glacier is a tidewater glacier which originates off the south face of Mount Saint Elias (5,489 m) and terminates just 19 km downstream. This steep relief in combination with the unique maritime climate leads to a high amount of orographic precipitation in its accumulation zone (Molnia, 2007).

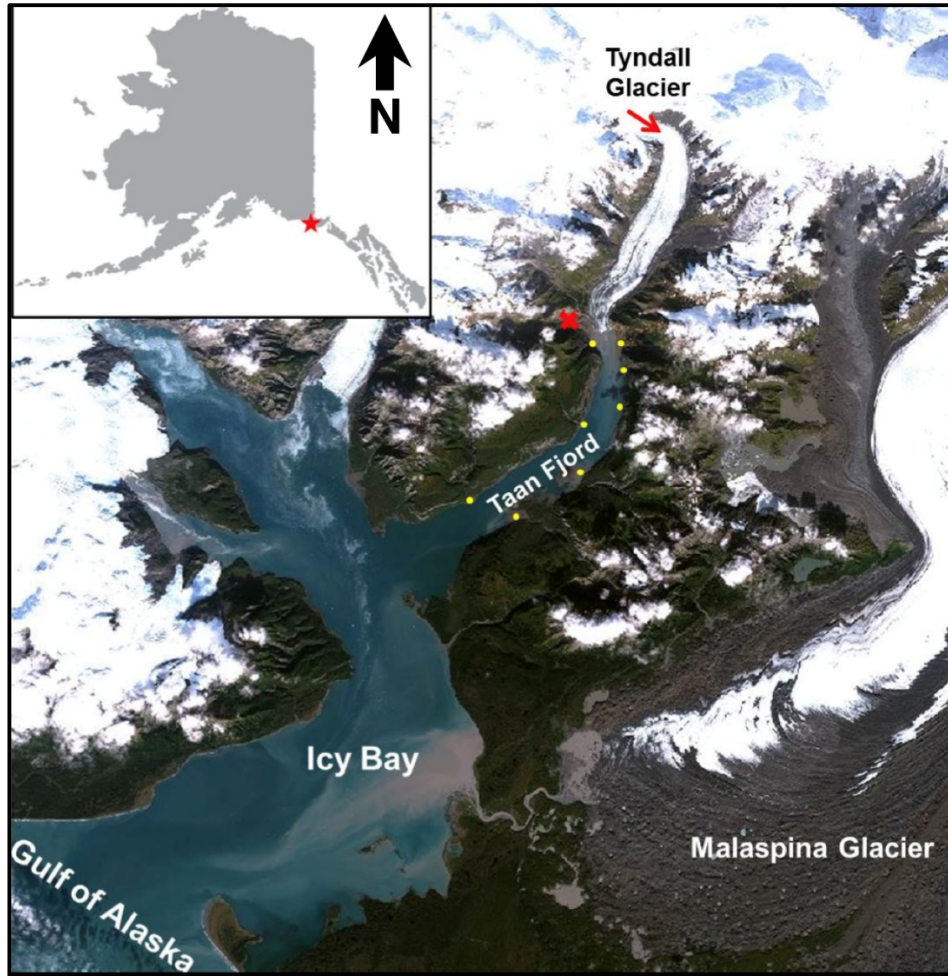


Figure 1-2. Icy Bay and Taan Fjord in Southeast Alaska on Copernicus Sentinel II (2017) base imagery. The yellow points represent each fan-delta analyzed in this study and the red x represents the location of the October 2015 landslide.

1.4.1 Glacial History

Tyndall Glacier retreated rapidly after it separated from the main trunk glacier in Icy Bay in 1961 (figure 1-3). Between 1961 and 1991, it retreated 17.25 km to its present position where its terminus remains stable due to a bedrock constriction (Koppes and Hallet, 2006). It retreated at a rate of $\sim 0.6 \text{ km yr}^{-1}$ between 1960 and 1969 (Koppes and Hallet, 2006). After 1969, a shallow bedrock sill located about 2 km up-fjord slowed the retreat of Tyndall Glacier to 0.15 km yr^{-1} (Koppes and Hallet, 2006). After 1983, the glacier entered the deeper northern basin of the fjord and retreated at an increased rate of $\sim 0.8 \text{ km yr}^{-1}$ until 1991 (Koppes and Hallet, 2006).

After 1991, the terminus fluctuated around its current position at the head of the fjord along the Chaix-Hills Fault due to a bedrock constriction (Koppes and Hallet, 2006; Meigs et al., 2006).

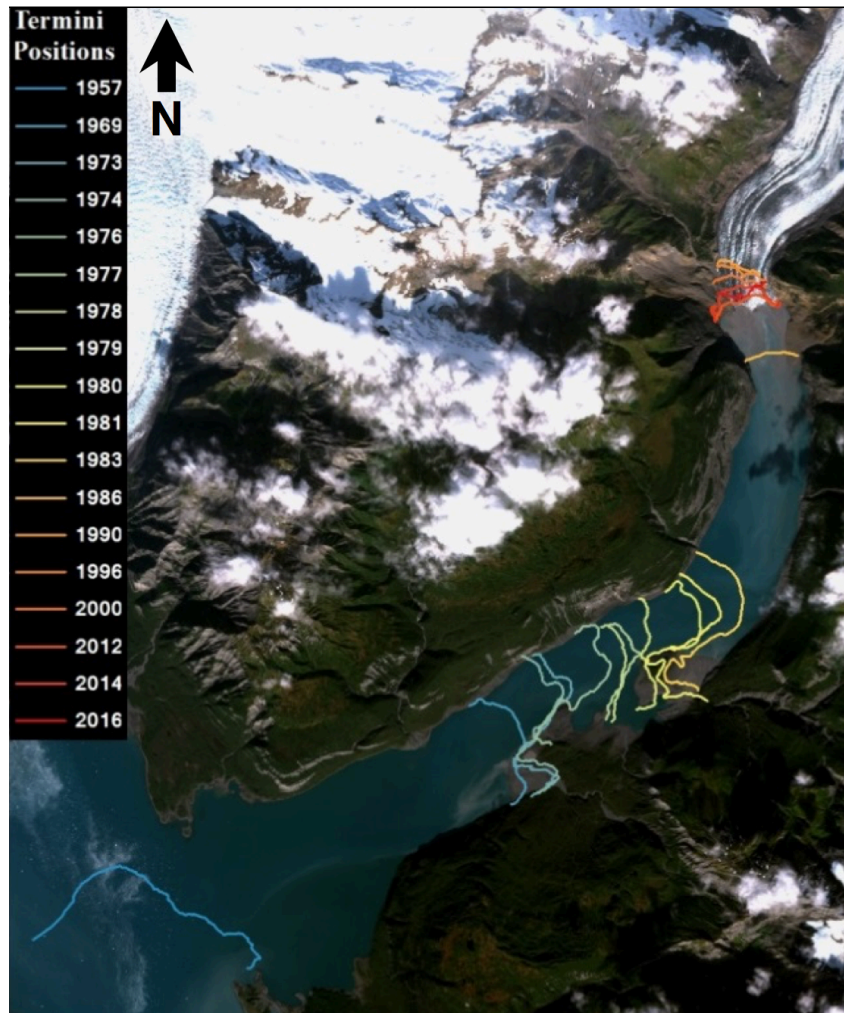


Figure 1-3. Tyndall glacier terminus positions.

1.4.2 Geology

The tectonic forces that created the highest coastal mountain range on earth (the St Elias Range) also have a profound and complex influence on Taan Fjord (figure 1-4). Taan Fjord sits on an actively accreting microplate which is bounded by major faults that include the strike-slip Fairweather Fault (Alaskan continuation of the Queen Charlotte Fault), expressions of the Aleutian megathrust fault, and the Chugach St. Elias thrust fault (Bruhn et al., 2004; Chapman et al., 2012; Chapman et al., 2011; Enkelmann et al., 2009; Larsen et al., 2005; Plafker et al., 1994;

Spotila et al., 2004). Numerous smaller faults also bisect Taan Fjord and Tyndall Glacier. Most notably, the Chaix-Hills thrust fault runs directly across the present-day terminus of Tyndall Glacier (Chapman et al., 2012). This region therefore has the potential to produce large- to great-magnitude earthquakes and experiences exhumation rates that rival those observed in the western Himalaya (Bruhn et al., 2004; Enkleman et al., 2009).

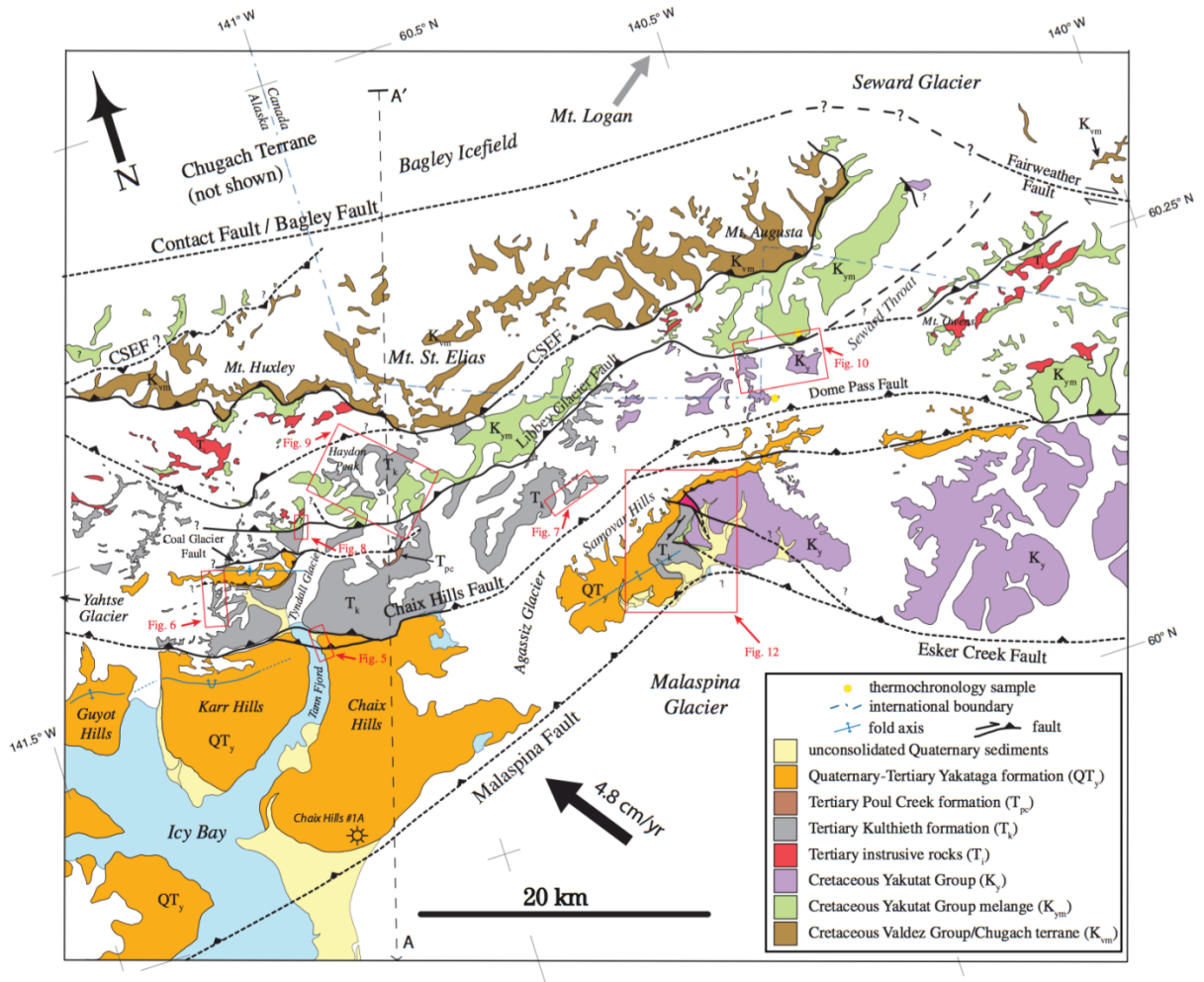


Figure 1-4. Fault systems around Icy Bay, the Malaspina Glacier and Bagley Icefield (Chapman et al., 2012). Taan Fjord is the located in the lower left of the figure.

The primary bedrock in Taan Fjord is an uplifted glacialmarine bedrock sequence known as the Yakataga Formation (Chapman et al., 2012; Eyles et al., 1991; Perry et al., 2009). Also present at the head of the fjord is the Poul Creek Formation, which underlies the Yakataga

Formation and is composed of highly-deformed marine mudstone and sandstone (Chapman et al., 2012; Eyles et al., 1991; Perry et al., 2009). Lastly, the Kulthieth Formation, an arkosic sandstone sequence interbedded with coal seams, primarily underlies Tyndall Glacier (Chapman et al., 2012; Perry et al., 2009). Outcrops are also found in the northernmost watershed of Taan Fjord (Chapman et al., 2012).

1.4.3 October 2015 Landslide

In October 2015, a 76 million m³ section of unstable rock collapsed into Taan fjord and partially on the terminus of Tyndall Glacier triggering a tsunami wave that was documented to be 192 m high at its maximum (Higman et al., in press). The effects of the tsunami were greatest at the head of the fjord, but the tsunami remained large enough to register on tide gauges in Yakutat 100 km away (Haeussler et al., in press). Runup at the mouth of Taan Fjord over 17 km from the landslide source exceeded 50 m (Bloom et al., 2017). The tsunami effectively stripped the vegetation from almost all of the low-lying fan-deltas in the fjord as well as along the fjord walls within several tens of meters of sea level. The remoteness of Taan Fjord meant that the landslide did not adversely affect people.

A main factor contributing to the occurrence of the 2015 landslide and induced tsunami was the effect of glacial debuttrressing on the failure slope. The slope was once buttressed by both Tyndall Glacier and one of its tributaries, Daisy Glacier. This buttressing effect was lost with the retreat of both glaciers and ultimately resulted in the pronounced weakening of the already weak sedimentary bedrock. We therefore consider this landslide a paraglacial event as it was indeed conditioned by deglaciation.

1.5 Study Goals

A unique opportunity existed in Taan Fjord that allowed us to witness the transition from a landscape dominated by glacial processes to one instead governed by paraglacial relaxation. The 2015 landslide event was a clear indication of landscape relaxation following Tyndall Glacier's rapid retreat, however interesting questions still remain about the smaller-scale unravelling processes happening in the eight tributary basins of Taan Fjord. It is clear that all of the tributaries had experienced a base-level fall from the retreat and thinning of Tyndall Glacier and that likely triggered incision in the lower reaches of the tributary streams. We sought to determine how much sediment was evacuated by these tributary watersheds by analyzing the fan-deltas at their outlets. We were also interested in finding the average sediment yields and basin-averaged erosion rates of the watersheds. These estimates could then be used to create a complete account of what happened during the beginning stages of the paraglacial period in the fjord, beyond what has been found by previous research into the sediment contributions from the landslide and Tyndall Glacier. In studying the evolution of Taan Fjord, we hoped to enhance our understanding of the potential magnitude of future landscape change facing other, similar glaciated regions around the world.

The goal of this thesis is to assess how the contributing basins to Taan Fjord have adjusted to the rapid retreat of Tyndall Glacier. Specifically, the following questions will be examined:

1. How has Tyndall Glacier retreated and thinned since its retreat from Icy Bay in 1961?
2. How have the tributary streams responded to the retreat of Tyndall Glacier?
3. How much sediment has accumulated in the fan-deltas of Taan Fjord since fan-delta formation began for each tributary?

4. How have sediment yields and erosion rates for each tributary basin changed through time?
5. How does the sediment yield and erosion rate from the tributary valleys compare to that from Tyndall Glacier and the October 2015 landslide?

1.6 Thesis Structure

This thesis aims to address the previously outlined research goals in a format consistent with standard scientific reporting and have the following chapters that reflect this format: methods, results, discussion and conclusion. Chapter 2 will highlight the methods used in this study, including structure from motion (SfM) photogrammetric techniques and the creation of the theoretical models used to estimate fan-delta size in the fjord. Chapter 3 will present the results of these analyses and Chapter 4 will be dedicated to the interpretation and discussion of the results. In this chapter, a comparison of the sediment contribution from the tributary valleys is made to that from Tyndall Glacier and the 2015 landslide. Additionally, a prediction of future landscape relaxation in Taan Fjord is presented. Finally, Chapter 5 summarizes the main findings of this thesis as they pertain to the research goals. A technical appendix will also be provided to offer more detail on complex SfM methodology.

Chapter 2: Methods

The retreat and thinning of Tyndall Glacier caused each of the tributaries in Taan Fjord to experience a base-level fall that led to pronounced incision in their lower reaches and the formation of deep canyons at their outlets. Therefore, determining the rate of terminus retreat and thinning is integral in placing not only a timeline on when fan-delta formation processes began for each basin, but also to determine the amount of base-level fall experienced by each tributary. This temporal and spatial information was used in the calculation of sediment yields and basin-averaged erosion rates for each watershed, thereby shedding light on the total magnitude of paraglacial processes active in each tributary since deglaciation began in Taan Fjord.

We decided to use several different methods to determine the amount of paraglacial relaxation in Taan Fjord in alignment with our above stated study goals:

1. To quantify the retreat and thinning of Tyndall Glacier, we used structure from motion photogrammetry to produce detailed Digital Terrain Models (DTMs) of the fjord before satellite imagery was available.
2. We used SfM DTMs, satellite-derived Digital Elevation Models (DEMS), LiDAR and historical aerial photographs to document and quantify the geomorphic evolution of the tributary streams.
3. We developed a volumetric model of the fan-deltas of Taan Fjord to obtain the total volume of sediment accumulated in each since they first began to form until 2016.
4. To obtain sediment yields and erosion rates for each tributary basin through time, we used the output from our volume models mentioned above and developed a relation between fan-delta surface area and volume. This allowed for the determination of volume

in the fan-deltas in historical photographs and imagery where only surface area information was available.

5. The final volumes, yields and erosion rates calculated for the tributary basins were compared to published volumes, yields and erosion rates for Tyndall Glacier and the 2015 tsunamigenic landslide (Dufresne et al., 2018; Haeussler et al., in press; Koppes and Hallet, 2006).

2.1 Glacier Thinning and Retreat

Tyndall Glacier's terminus positions were updated from Koppes and Hallet (2006) to include the years between 2000 and 2017 (figure 1-3; table 2-1). All surface analyses were conducted in ESRI's ArcGIS unless otherwise noted. Structure from motion photogrammetry was performed in Agisoft PhotoScan to reconstruct 3-dimensional DTMs of the glacier surface using historical aerial photographs from which ice thicknesses were determined. Details on the methods and error quantification of the SfM technique used in this study are provided in Appendix I.

In each SfM DTM, cross sections were run across the fjord at the location of each tributary's modern-day outlet to quantify ice thickness changes and thereby base-level fall for the tributary basins during Tyndall Glacier's retreat. We assumed that the glacier surface represented base-level for each tributary until the glacier retreated completely past their outlets and base-level became sea level. The changes in ice elevation over time was used to calculate a rate of base-level fall for each tributary.

Date	Imagery Type	Resolution (m)	Imagery Source
7/1957	SfM DTM	1	USGS: unknown
7/1957	SfM Orthoimage	1	USGS: Austin Post
8/1969	SfM DTM	1	USGS: Austin Post
8/1969	SfM Orthoimage	0.38	USGS: Austin Post
9/1973	SfM DTM	1	USGS: Austin Post
9/1973	SfM Orthoimage	0.5	USGS: Austin Post
9/1986	SfM DTM	1	USGS: Austin Post
9/1986	SfM Orthoimage	0.38	USGS: Austin Post
7/1994	Landsat 4-5	30	USGS
7/1998	Landsat 4-5	30	USGS
8/2000	IfSAR DEM	5	Geographic Information Network of Alaska (GINA)
8/2006	Landsat 4-5	30	USGS
11/2012	DEM	2	ArcticDEM
2/2014	DEM	2	ArcticDEM
3/2014	DEM	2	ArcticDEM
9/2014	Satellite Image	0.5	Worldview-2
5/2016	DEM	2	ArcticDEM
6/2016	DEM	2	ArcticDEM
6/2016	LiDAR	0.2	Chris Larsen (University of Alaska Fairbanks)
6/2016	Orthoimage	0.1	Chris Larsen (UAF)
8/2016	DEM	2	ArcticDEM
8/2016	Bathymetry (DEM)	1	USGS
9/2017	Satellite Image	10	Copernicus Sentinel Data

Table 2-1. Imagery used for glacier and tributary basin analyses. SfM DTMs are surfaces constructed from multiple aerial photos (see Appendix I for details on SfM technique).

2.2 Watershed Delineation and SfM

Eight watersheds and their fan-deltas make up the paraglacial landscape in Taan Fjord and were named according to the date their basin outlets were first exposed following the retreat of Tyndall Glacier (figure 2-1). These years represent the first year base-level was equivalent to sea level and when fan-delta progradation began in the fjord for each tributary. The fan-deltas

were digitized visually using a 5 m IfSAR DEM from 2000 (table 2-1), its associated hillshade and contour, and Google Earth. Ridgelines and differences in slope and aspect were identified and interpreted to include the most likely areas contributing water and sediment to each tributary watershed.

As defined by Nemeč and Steele (1988), “a fan-delta is a prism of sediments delivered by an alluvial fan and deposited, mainly or entirely subaqueously, at the interface between the active fan and a standing body of water”. Using this definition, the fan-deltas were delineated using a combination of LiDAR imagery (UAF, 2016) and multibeam bathymetry collected by the US Geological Survey (USGS) research vessel *Alaskan Gyre* in May 2016 (table 2-1). They were identified visually from a 2016 orthophoto and by their contours which were convex in the direction of flow. In addition to generated contours, hillshades were also created to further determine the extent of the features. The apex of each fan-delta was considered to be at the location of the first indication of deposition. This point of transition was identified both by confirming visually where deposition began and also where contours transitioned from concave to convex. This was typically a distinct point where the streams emerged onto the subaerial fan from incised canyons. The subaqueous fan-delta fronts were clear in the bathymetry as a sudden break in slope from the steep delta surfaces to the relatively flat fjord bottom. The fan-deltas were subdivided into their respective subaerial and subaqueous parts at the mean higher high water (MHHW) tide line. The MHHW tide line was identified visually in the 2016 orthophoto and was clearly discernible by a sharp boundary between dry and wetted, yellow-algae-covered sediment on the perimeter of the subaerial fan fronts.

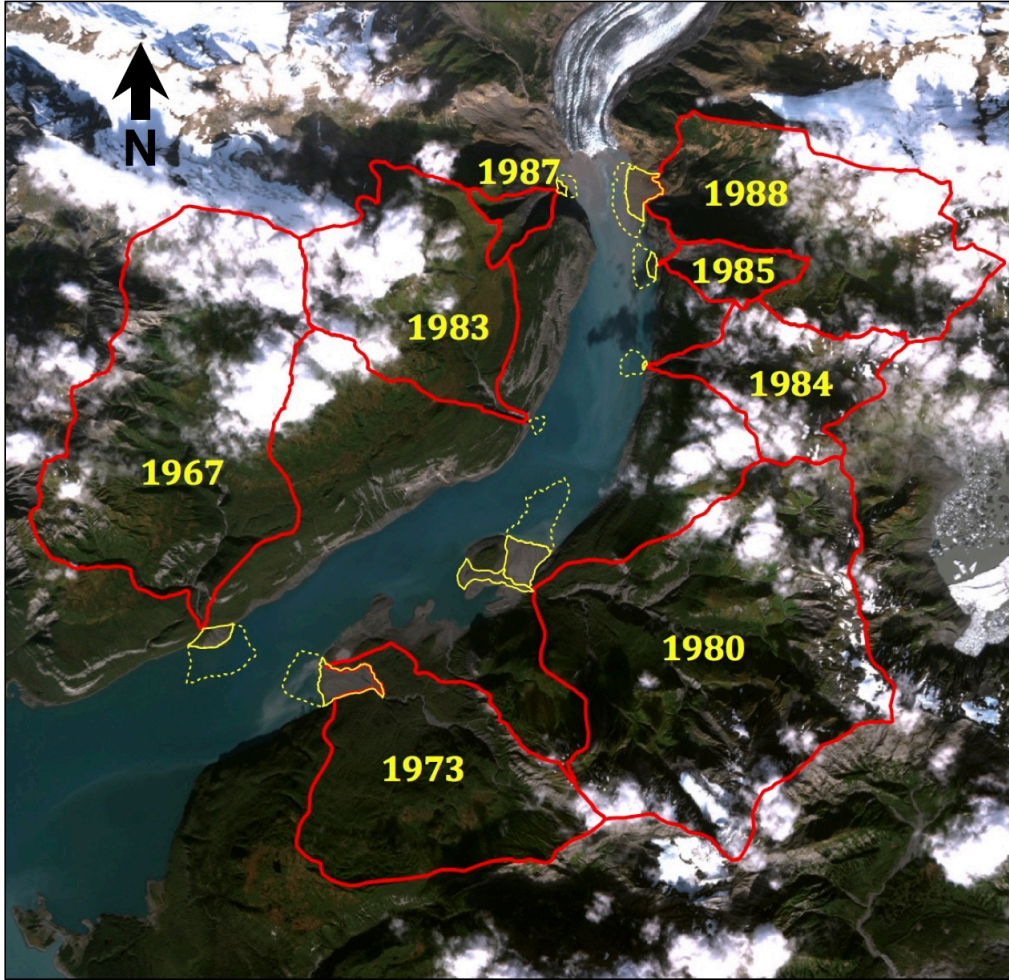


Figure 2-1. Tributary watersheds and fan-deltas of Taan Fjord named according to the exposure date of their basin outlets following Tyndall Glacier’s retreat. Watersheds are outlined in red, subaerial portions of fan-deltas are solid yellow, and subaqueous portions of fan-deltas are dotted yellow.

SfM DTMs were constructed of the land surface in Taan Fjord using historical aerial photographs (Appendix I). These DTMs, in addition to satellite-derived DEMs, were used to construct longitudinal profiles for each tributary stream. To create the profiles, 3-dimensional transect lines were manually drawn down the visibly active channel for all streams in all available DTMs/DEM to where the stream either flowed directly into the glacier, an ice-marginal lake, or the ocean. The lines were drawn to the extent of coverage in the DTM or DEM, which in some years meant the headwaters of some stream profiles were not captured.

2.3 Volume Models

The original volumes contained within the fans in 2016 provided the foundation for our sediment yields and basin-averaged erosion rates. It would be these volumes that would be used to determine sediment yields and basin-averaged erosion rates for each tributary basin. Thus, total volume within each fan-delta was obtained using a Monte Carlo (MC) analysis on three geometric models of the fan-deltas as they appeared in 2016 imagery (figure 2-2). All of the fan deltas were assigned to one of the three geometries and each was divided down into equal segments with a length, width, and height. These segments were then summed to provide an estimate of total volume using the basic equation:

$$V = \sum_{i=1}^N l_i \cdot w_i \cdot h_i$$

[1]

where N represents the user-defined segments to sum volumes across, and l_i , w_i , and h_i are the length, width, and height of each segment respectively. For each of the models, the number of segments, N , was 10,000. Determining the length, width, and height variables for each model varied and is discussed in detail below.

Two of our models required 7 input variables to determine volume and one model required 8 input variables (table 2-2). We thought that assigning exact values to these variables and determining error after the fact would be too subjective and inaccurate. Instead, potential errors were calculated directly within the model using a MC simulation. To do so, the maximum and minimum value for each variable was specified and a random uniform distribution was created using these values as bounds. This meant that each possible value between these bounds

had an equal likelihood of being correct. Finding these minimum and maximum bounds for each variable is discussed below in the error analysis section.

The frequency of data points in each uniform distribution was 100,000. These uniform distributions were then used as the variable inputs into a MC simulation instead of a single, static value to produce a distribution of likely volumes for each fan and its associated model. The number of simulations in each MC run was 100,000.

Model Parameter	Definition	Models Using Parameter
N	number of segments to calculate volume for (N = 10,000)	1, 2, 3
θ	splay angle of the fan apex (rad)	1, 2, 3
β	average gradient of the delta and subaqueous foreset bed angle (rad)	1, 2, 3
r	radius of subaerial fan from apex to sea level (m)	1, 2, 3
z	elevation of the apex of the fan (m)	1, 2, 3
d	depth of the delta toe (m)	1, 2, 3
S_f	fjord wall gradient and fjord wall gradient under subaerial fan-delta 1973 (rad)	1, 2, 3
S_{f2}	fjord wall gradient under subaqueous fan-delta 1973 (rad)	3

Table 2-2. Model parameters needed to obtain volumes for the fan-deltas of Taan Fjord.

2.3.2 Geometry

In profile, the subaerial surfaces of all the fan-delta models have a lower gradient than their delta surfaces, thereby creating a pronounced break in slope at sea level where these two segments meet. This is due to the ability for granular deposits to hold a higher angle of repose in water than in air. The average subaerial fan gradient was determined by taking the height of the fan at its apex, z , and dividing by the radius of the subaerial fan, r . The subaqueous gradient was found by taking the average gradient across the subaqueous delta surface in ArcGIS and was then assumed to be the angle of the foreset beds, β .

The underlying fjord wall geometry for the fan-deltas was assumed to be a continuation of the average gradient of the fjord wall on either side of the subaqueous deltas. With the

exception of fan-delta 1973, this manifested as a simple inclined plane underlying all fan-deltas that terminated at a horizontal basal plane. The basal plane for all fan-deltas was assumed to be at the average delta-toe depth. This assumes that accumulation of sediment in the fjord bottom from Tyndall Glacier was constant.

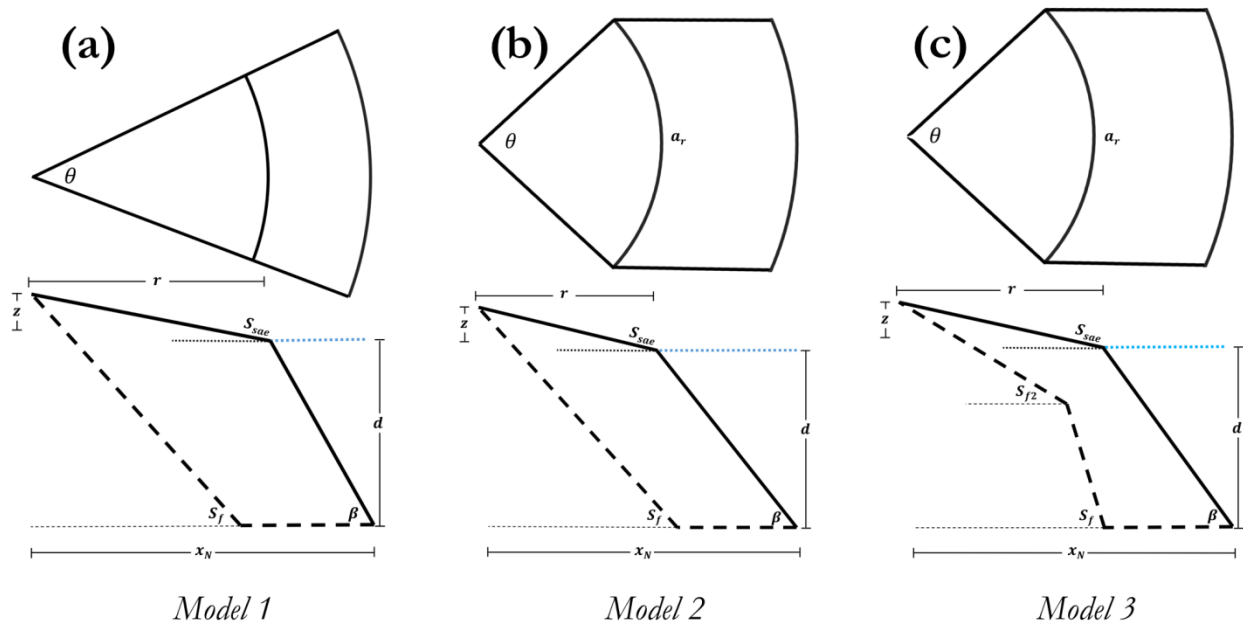


Figure 2-2. Fan-delta geometries across the three different models: (a) represents a fan-shaped wedge of sediment that increases in width with increased distance from the fan apex, (b) depicts those fans that stop increasing in width at sea level, and (c) shows a geometry similar to (b), but with a convex bedrock geometry.

2.3.2.1 Fan-Delta Model 1

The first model is the simplest of all three models. This fan-delta type is assumed to be a fan-shaped wedge of sediment that increases in width with increased distance from the fan apex (figure 2-2a). The only fan-deltas exhibiting this shape were fan-deltas 1983 and 1988 and their volumes were found using the equation:

$$V_1 = \sum_{i=1}^N (\theta * x_i) * (x_2) * (h_i - hb_i)$$

[2]

where θ is the splay angle of the fan at its apex and x is the horizontal distance from the fan apex to delta toe along the base of the fan-delta from $i = 1$ to N number of segments. h is the elevation of the fan-delta surface and hb_i is the elevation of the underlying bedrock surface. x_2 is the horizontal distance between the apex of the fan and start of the second segment and thus represents the width of each segment. The total length of x is given by:

$$x = r + d(\tan\beta) \quad [3]$$

where d is delta toe depth and r is the radius of the subaerial fan. β is the foreset bed angle.

The elevation of the fan-delta surface above the delta toe, h , is composed of two elevation vectors: h_{sae} for the elevation of each segment of the fan above sea level (subaerial heights) and h_{saq} for elevation of each segment of the delta surface below sea level (subaqueous heights) and can be seen in more detail in figure 2-3. These two variables were found by:

$$h_{sae} = \sum_{i=1}^r (r - x_i) * S_{sae} + d \quad [4]$$

$$h_{saq} = \sum_{i=r}^N d - (x_i - r) * \tan(\beta) \quad [5]$$

where S_{sae} is the slope of the subaerial fan (m/m) obtained by dividing the fan apex elevation, z , by the subaerial radius, r . This h variable is the height of the surface of the fan-delta above the delta toe elevation, and so the geometry of the fjord wall must be subtracted from these heights to prevent including bedrock in the volume estimations. The elevation of the fjord wall beneath the fan-delta, hb_i , is given by the linear function:

$$hb_i = \sum_{i=1}^N (z + d) + S_f * x_i$$

[6]

where S_f is the assumed slope of the fjord wall, z is the fan apex elevation, and d is average depth of the delta toe.

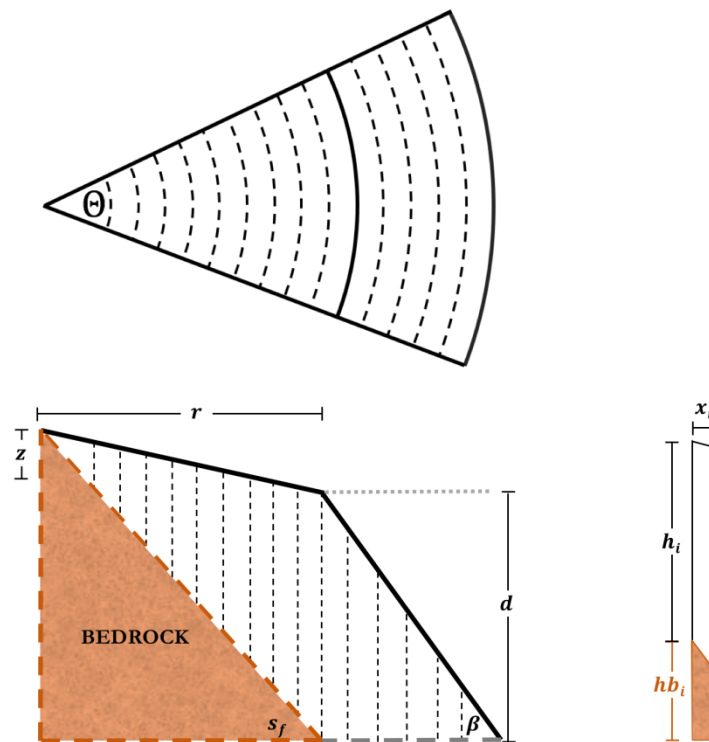


Figure 2-3. Detailed depiction of variables involved in volume model 1. The top image shows the fan-delta in planview and the lower two images depict the fan-delta in profile. The column on the lower right represents one segment. The sum of the volume found in all the segments ($N=10,000$) provides a total volume estimate for the fan-delta.

As a note, volume for fan-delta 1983 was also calculated using this model, however this fan-delta is completely subaqueous. To account for this, the input for radius of the subaerial fan-delta, r , was simply 0 m. The model therefore only considered volumes below sea level for fan-delta 1983.

2.3.2.2 Fan-Delta Model 2

Five of the fan-deltas had a geometry similar to that of figure 2-2b. These deltas are characterized by a fan-shaped wedge of sediment above sea level, but below sea level the width of the fan does not increase. Fan-deltas 1967, 1980, 1984, 1985, and 1987 all fit this category of fan-delta. The formula for model 2 is almost exactly the same as that of model 1, however the radial increase of each segment stops at sea level and remains the same until the delta toe. Thus, the equation looks similar to equation 2:

$$V_2 = \sum_{i=1}^N (a_i) * (x_2) * (h_i - hb_i)$$

[7]

with the only difference being in the use of a . In this case, a_i is an arclength that consists of two vectors, a_{sae} and a_{saq} . They account for the termination of radial increase at sea level and a_{sae} is found by:

$$a_{sae} = \sum_{i=1}^r \theta * (r - x_i)$$

[8]

which creates a fan shape of increasing arc length components with increasing distance from the fan apex until the radius of the subaerial fan, r , is reached. a_{saq} is simply a repetition of the final value of a_{sae} until the distance to the delta toe is reached:

$$a_{saq} = \sum_{i=r}^N \theta * r$$

[9]

2.3.2.3 Fan-Delta Model 3

Model 3 was only used on fan-delta 1973 and it uses elements of both model 1 and 2. It has the same geometry as model 2, however the fjord wall underneath the fan delta has a convex shape instead of a simple linear shape (figure 2-2c). Volume for fan-delta 1973 was thus found by summing the volume of the subaerial and subaqueous portions of the fan separately:

$$V_3 = V_{sae} + V_{saq} \quad [10]$$

To find the subaerial volume, V_{sae} , we used:

$$V_{sae} = \sum_{i=1}^r \theta * (r - x_i) * (x_2) * (h_i - hb_i) \quad [11]$$

This equation is essentially the same as equation 2, but it terminates the calculation of volume at sea level, thus only obtaining subaerial volume.

For the subaqueous volume, V_{saq} , we assumed that there was no radial increase below sea level for this fan, as we did in model 2. We therefore used an equation similar to equation 7 to find the subaqueous volume:

$$V_{saq} = \sum_{i=r}^N (a_{saqi}) * (x_2) * (h_i - hb_i) \quad [12]$$

In both equations, h still represents a vector of the elevation of the surface of the fan-delta above the delta toe, only h in equation 11 is the elevation above sea level and h in equation 12 is the elevation below sea level of each segment. The elevation of the fjord wall beneath the fan, hb_i , in both equations 11 and 12 is found by a linear function representing the fjord wall geometry, as

was detailed in equation 6. There are two different fjord wall slopes, S_f and S_{f2} , that were applied in this model and so hb_i will take on different values for each equation. The fjord wall slope under the subaerial portion is less than that under the subaqueous portion, thereby producing a prominent break beneath the fan-delta (figure 2-2c).

2.3.3 Error Analysis

The bounds of the uniform distributions for each variable that were used in the MC volume calculations were determined in various ways and are displayed in table 2-3. We determined the minimum and maximum splay angle of the fan-deltas at their apexes, θ_{\max} and θ_{\min} , by measuring angles of what we deemed to be reasonable and cautious extremes. As an example, if a fan-delta had a measured θ of 140 degrees, it would be unreasonable to surmise that the true θ could be any value between a θ_{\max} of 180 degrees and θ_{\min} of 90 degrees. Conversely, it would be imprudent to have a θ_{\max} of 145.5 degrees and θ_{\min} of 139.5 degrees because they are too small of bounds to represent a conservative breadth of error. Therefore, based on the actual measurement of 140 degrees, it would be plausible that the true θ could be any value between a θ_{\max} of 150 degrees and a θ_{\min} of about 130 degrees. While it would be unlikely that the measurement of the apex angle was off by ± 10 degrees, we believe these estimates would provide a large enough range to safely account for measurement errors and encompass the true θ .

For the subaqueous gradient/foreset bed angles, β_{\max} and β_{\min} , multiple 3-dimensional transect lines were run down the delta front and a distribution of average gradients was created. β_{\max} was the maximum gradient of that distribution and β_{\min} was the minimum gradient.

The minimum and maximum radius of each fan-delta was determined by creating several lines drawn from the fan apex to the edge of the subaerial fan for each fan-delta. They were

drawn where it appeared the true radius most likely resided. We took the maximum possible length for r_{\max} and the minimum length for r_{\min} . Again, our estimates of the minimum and maximum were conservative to ensure we captured the true radius.

The fan-deltas of Taan Fjord interfinger with glacigenic sediment from Tyndall Glacier for some distance below the sea bed. For this reason, the maximum depth, d_{\max} , was found using isopach maps of the basement bedrock from Haeussler et al. (in press) and Koppes and Hallet (2006). It was assumed that each fan-delta began to prograde on this basement bedrock while simultaneously starting to interfinger with glacigenic sediment coming from Tyndall Glacier, and so the maximum depth was considered to be between 10 and 50 m below the surface depending on the location of each fan-delta. The minimum depth, d_{\min} , was the average depth of the fan front where it intersected sea bed.

The fjord slope gradient beneath the fan deltas was determined using the same methods as were used to find β_{\max} and β_{\min} . Transect lines were run down the fjord walls directly adjacent to the fan-deltas and a distribution of the average gradients was created. The minimum and maximum of that distribution was taken as the $S_{f\max}$ and $S_{f\min}$. The same methods were used to find $S_{f2\max}$ and $S_{f2\min}$, only these variables represented the underlying slope of the subaerial component of the 1973 fan-delta.

	Description	FD 1967	FD 1973	FD 1980	FD 1983	FD 1984	FD 1985	FD 1987	FD 1988
θ_{\max}	Max fan apex splay angle	2.59	0.66	0.87	1.67	2.50	2.79	2.22	1.39
θ_{\min}	Min fan apex splay angle	2.42	0.48	0.70	1.47	2.00	2.40	1.90	1.00
β_{\max}	Max foreset bed angle	0.47	0.57	0.23	0.85	0.83	0.86	0.84	0.82
β_{\min}	Min foreset bed angle	0.38	0.38	0.13	0.82	0.71	0.63	0.70	0.60
r_{\max}	Max radius of subaerial fan	383.28	1244.57	914.30	0	61.21	187.07	169.71	694.63
r_{\min}	Min radius of subaerial fan	344.12	1227.86	888.43	0	58.90	185.57	153.70	676.40
z	Elevation of fan apex	20.65	26.03	26.08	0	6.62	25.38	29.70	66.63
d_{\max}	Max depth of fan front	158.53	152.11	110.53	151.22	133.33	140.94	81.28	131.41
d_{\min}	Min depth of fan front	118.53	112.11	100.53	101.22	103.33	100.94	71.28	101.41
$S_{f\max}$	Max fjord wall slope	-0.35	-0.52	-0.10	-1.12	-0.63	-0.72	-0.79	-0.25
$S_{f\min}$	Min fjord wall slope	-0.45	-0.78	-0.13	-1.51	-0.71	-0.82	-0.97	-0.35
$S_{f2\max}$	Max subaqueous fjord slope	---	-0.106	---	---	---	---	---	---
$S_{f2\min}$	Min subaqueous fjord slope	---	-0.108	---	---	---	---	---	---

Table 2-3. Maximum and minimum values used for model parameters. Elevation of the apex was considered to be accurate and thus no minimum or maximum was used for z .

2.4 Sediment Yields and Erosion Rates

Alluvial fans share a constant volume-area proportionality with increased growth that follows a power-law trend (Giles et al., 2010). This suggests that as the fan-delta grows in surface area, its volume also grows in constant relation to that area increase. Therefore, to generate sediment yields for the basins in Taan Fjord, we calculated the total volume of the fan-deltas in 2016 using the volume models described previously and created a constant of proportionality between the observed fan-delta area and modelled fan-delta volume. Then, a subaerial to subaqueous surface area ratio was found for each fan-delta in 2016 and used to

determine total surface areas in years when no bathymetric data existed. Finally, the total area derived from this ratio was multiplied by the surface area-to-volume relation for each fan-delta in the year of interest (figure 2-4; table 2-4). This allowed for an estimation of fan-delta volume in historical aerial imagery in which only subaerial components of the fan-deltas were visible. Doing so yielded a volume that could then be used to calculate sediment yield and basin-averaged erosion rates in the tributary watersheds over the last half a century.

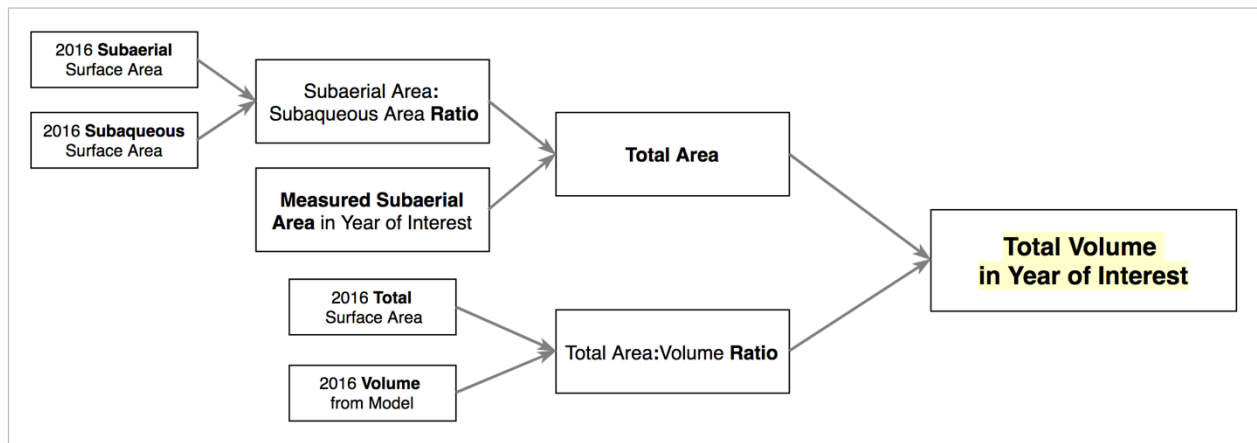


Figure 2-4. Flowchart of methods used to obtain fan-delta volumes from subaerial surface areas.

	Subaerial/Subaqueous Proportionality Constant	Area/Volume Proportionality Constant
FD 1967	0.30	0.022
FD 1973	1.07	0.012
FD 1980	0.99	0.033
FD 1984	0.04	0.39
FD 1985	0.30	0.029
FD 1987	0.35	0.034
FD 1988	1.14	0.019

Table 2-4. Surface area ratios and area to volume ratios that were used for each fan-delta to obtain volumes in years that lacked enough data to be used in the model for volume calculation.

We then compared these volume estimates to the timeline of fan-delta progradation for each tributary. The timeline of fan-delta progradation was determined by finding the initial date

of exposure of the basin outlet in historical aerial photos (i.e. the year when the terminus retreated past the outlet). Then, sediment yields were calculated using the equation:

$$Y = \frac{dV}{dt} \quad [13]$$

where Y is basin sediment yield, dV is the change in volume since the last year of measurement, and dt is the amount of time that passed since the last year of measurement.

Basin-averaged erosion rates were found using:

$$\dot{E} = \frac{\left[\frac{\rho_R}{\rho_S}\right] \cdot Y}{A} \quad [14]$$

where \dot{E} is the basin-averaged erosion rate, ρ_R is the density of the bedrock which was assumed to be 2350 kg m^{-3} for the dominant bedrock (Yakataga Formation) in Taan Fjord (Haeussler et al., in press), ρ_S is the density of saturated fan-delta sediment that was assumed to be 1600 kg m^{-3} (Pelkola and Hickin, 2004; Tunnicliffe et al., 2012), Y is the sediment yield obtained from equation 13, and A is the watershed area.

Chapter 3: Results

The thinning and retreat of Tyndall Glacier spurred a reaction in all tributary watersheds of Taan Fjord as they attempted to adjust to a new equilibrium with sea level as their base level. The tributary streams responded by making vertical adjustments via incision into their channels and also lateral adjustments where they weren't confined to narrow bedrock canyons. These changes often created knickpoints that migrated several kilometers per year or were completely reworked altogether. While the type of geomorphic changes in the basins varied, the rate of change was extremely rapid for almost all tributaries. This fast pace of change was reflected in the total volume of sediment accumulated in the fan-deltas of Taan Fjord, as well as their associated average annual sediment yields and basin-averaged erosion rates.

3.1 Thinning Rates

Tyndall Glacier's terminus retreat was accompanied by rapid surface thinning (figure 3-1). Thinning along the fjord walls essentially led to a drop in base level for the tributary streams from the glacier surface to the sea level. When the glacier filled the fjord in 1957, its thickness at the entrance of the fjord was over 400 m and over 650 m at the current terminus.

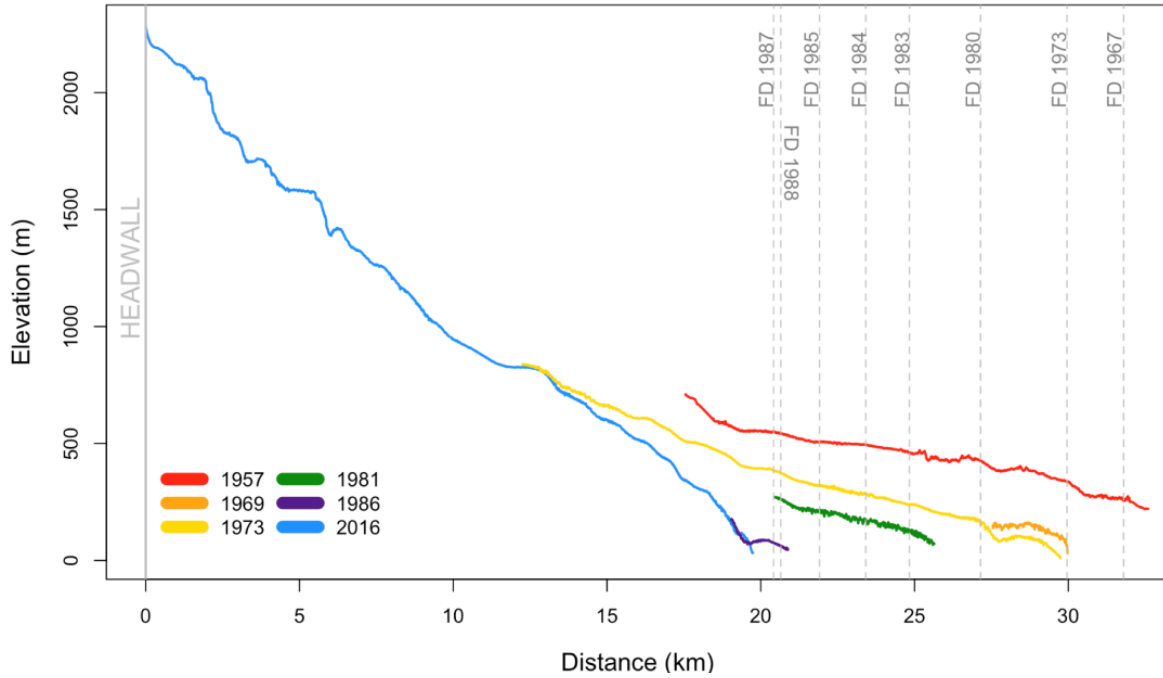


Figure 3-1. Centerline elevation of Tyndall Glacier from 1957 – 2016. There was limited coverage in some imagery, with 2016 being the only complete profile. Where the 2016 profile (blue) terminates is the location of a bedrock constriction that has kept the terminus of Tyndall Glacier relatively stable. Vertical dashed lines indicate locations of tributary outlets along this centerline.

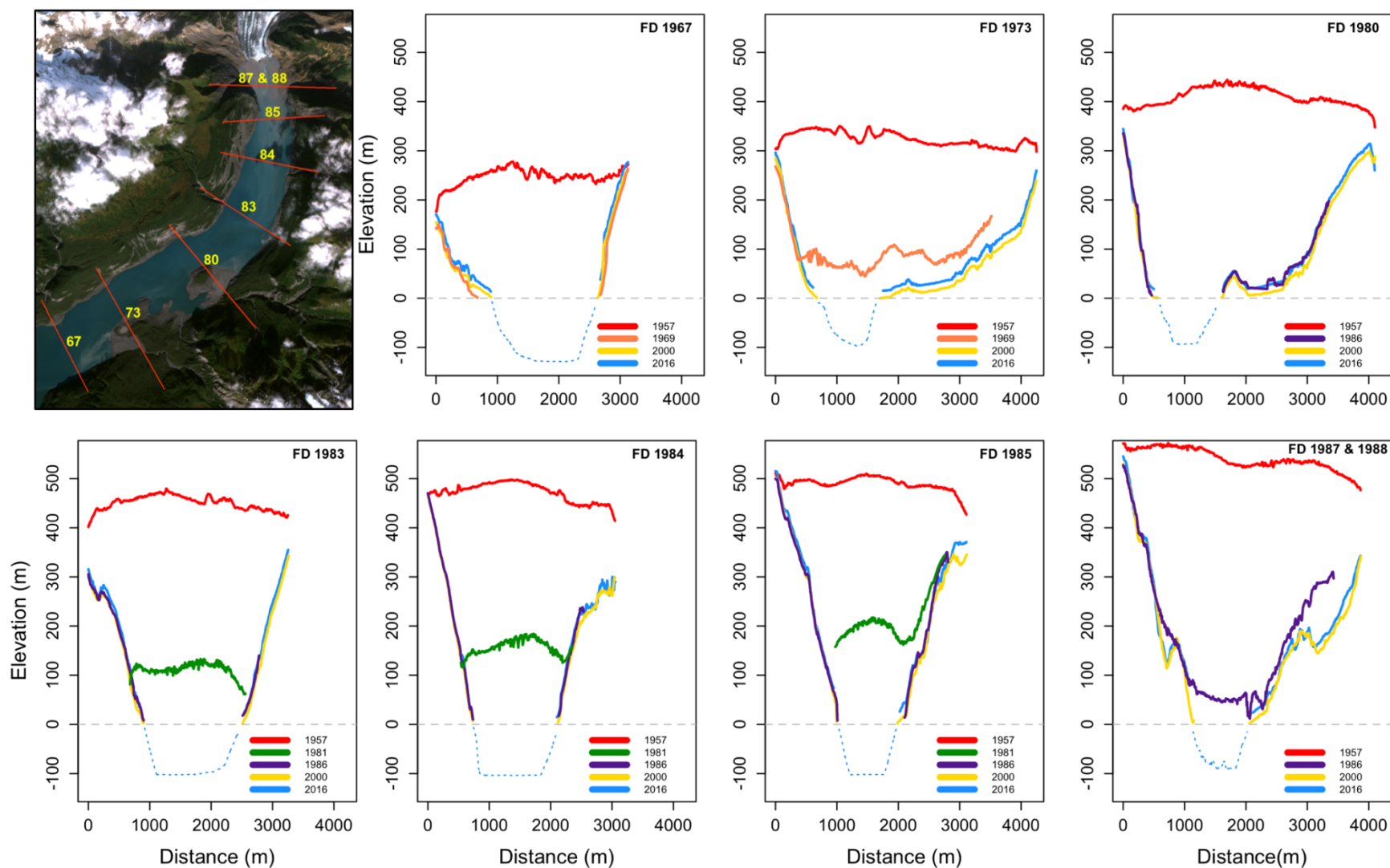


Figure 3-2. Cross sections across the fjord at the location of each tributary outlet from 1957 – 2016. Map of the cross sections also labelled in the first panel. Cross sections detail the surface from the west side of the fjord to the east side. The lengths of the cross sections are the exact width of the 1957 glacier surface and interpolated across all available years of imagery. All graphs are placed on the same scale, highlighting the differences in ice thickness and base level fall across the different tributaries.

	Base Level Fall since 1957 (m)	Average Rate of Fall since 1957 (m yr⁻¹)
FD 1967	177 ± 6	18 ± 0.6
FD 1973	298 ± 6	20 ± 0.4
FD 1980	347 ± 6	15 ± 0.3
FD 1983	402 ± 6	15 ± 0.2
FD 1984	414 ± 6	15 ± 0.2
FD 1985	427 ± 6	15 ± 0.2
FD 1987	572 ± 6	19 ± 0.2
FD 1988	476 ± 6	15 ± 0.2

Table 3-1. Total base level fall and average rate of fall for all tributaries.

The average rate of fall for each tributary was found by dividing the total fall by the number of years since 1957 before the outlet was exposed. The amount error in the base-level fall estimates was derived from the average error found in the 1957 DTM (see Appendix I for details on SfM error methods). The proportion of error in the total base-level fall for each tributary was applied to the rate of fall estimates to obtain errors for the rates.

Fan-delta 1987 experienced the greatest base-level drop (572 ± 6 m) and fan-delta 1967 the least (177 ± 6 m). The average rate of base level drop since 1957 until the year the outlet was exposed to the water surface (0 m) varied between 15 and 20 m yr⁻¹ for all tributaries. Those tributaries at the head of the fjord experienced an overall greater base level drop than those at the entrance of the fjord (figure 3-3; table 3-1). On average, the upper tributaries located where the walls on either side of the fjord are steep (watersheds 1983, 1984, 1985, 1986, and 1988) experienced a base level drop of 458 ± 6 m. Those tributaries closest to the entrance of the fjord where the fjord walls are gentler-sloped (watersheds 1967, 1973, and 1980) experienced an average base-level fall of 274 ± 6 m. Taken together, the average base-level fall for all the tributaries is 389 ± 6 m.

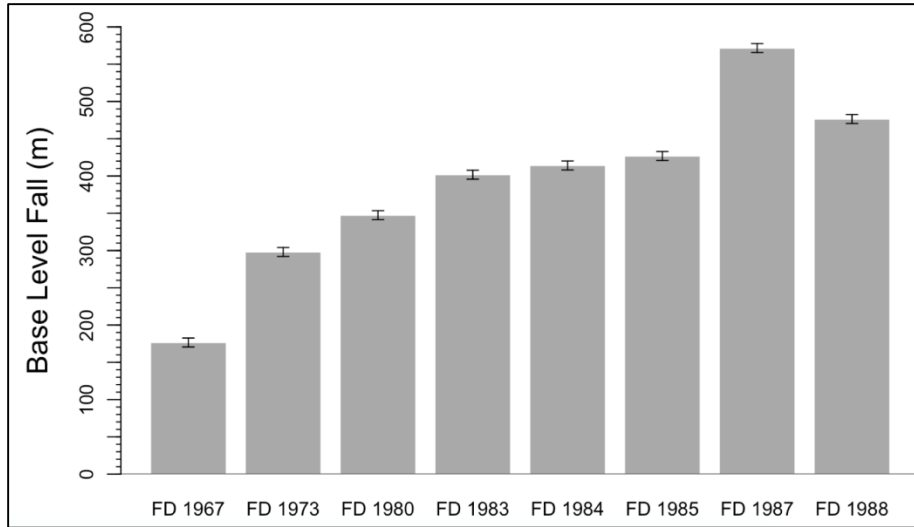


Figure 3-3. Total base level fall at the outlet of each tributary watershed since 1957.

3.2 Tributary Watersheds

3.2.1 Watershed Characteristics

In 2016, stream 1967 was the longest at 7.62 km and stream 1987 was the shortest at just 1.14 km. Watershed 1987 also had the steepest subaerial gradient of 15.46° and smallest basin size at less than 1 km^2 . Stream 1980 was $\sim 0.18 \text{ km}$ shorter than stream 1967, making it the second longest of the tributary streams but its watershed was the largest at 23.7 km^2 . Fan-delta 1980 also had the lowest subaerial (3.73°) and subaqueous gradients (9.83°), whereas the highest gradient (25.18°) was observed for the smallest fan-delta (0.04 km^2) at the outlet of watershed 1983. Descriptive characteristics of each basin can be seen in table 3-2

	1967	1973	1980	1983	184	1985	1987	1988
<i>Fan-Delta Characteristics</i>								
Years Exposed	49	43	36	33	32	31	29	28
Area (km ²)	0.73	0.85	1.18	0.04	0.13	0.21	0.09	0.60
Depth of Fan Front b.s.l. (m)	118.53	112.11	100.53	101.22	103.33	100.94	71.28	101.41
Avg. Subaerial Gradient	11.80°	3.81°	3.73°	---	8.29°	14.03°	15.46°	9.90°
Avg. Subaqueous Gradient	15.58°	14.42°	9.83°	25.18°	16.07°	22.87°	20.45°	19.38°
Apex Elevation a.s.l. (m)	20.65	26.03	26.08	0	6.62	25.38	29.70	66.63
<i>Stream Characteristics</i>								
Total 2016 Length (km)	7.78	6.24	7.60	4.94	3.59	2.96	1.14	7.18
Length added since 1957 or 1986 (km)	0.95	3.30	3.56	0.10	1.09	1.67	0.23	2.38
Knickpoint Migration (km)	---	0.48	0.70	---	---	0.34	---	2.22
Knickpoint Migration Rate (m yr ⁻¹)	---	11.26	16.30	---	---	8.00	---	51.63
<i>Watershed Characteristics</i>								
Watershed Area (km ²)	19.7	11.9	23.7	9.6	5.4	1.6	0.9	12.1
Average Gradient	28.09°	20.12°	25.70°	24.31°	23.27°	34.16°	31.98°	26.13°
<i>Geology</i>								
Lithology	Yakataga	Yakataga	Yakataga	Yakataga	Yakataga	Yakataga/ Poul Creek	Yakataga	Yakataga/ Kulthieth/ Poul Creek
Chaix-Hills Thrust Fault?	Not present	Not present	Not present	Present	Not present	Present	Present	Present

Table 3-2. Fan-delta, stream, and watershed characteristics as well as general geologic setting for each tributary basin.

3.2.2 Morphological Evolution

The evolution of the tributary watersheds began in 1957 with their outlets being blocked by Tyndall Glacier. The watersheds of tributaries 1984, 1985 and 1987 were almost completely filled with ice from Tyndall Glacier at this time. Dominant features present in six of the watersheds in 1957 were ice-marginal lakes that varied in size between tributaries. The largest ice-marginal lake was located in watershed 1980 and the smallest in watershed 1967. There was evidence seen in aerial photographs that lake levels were higher for watersheds 1973, 1980, and 1988 at some point before 1957, as grounded icebergs were observed above the 1957 shoreline.

After 1957, drawdown in ice volume of Tyndall Glacier began to drop base-level for the tributaries and those basins at the entrance of the fjord were the first to be affected. The streams began to lengthen as glacier thinning caused a drop in the surface elevation of the ice on the fjord walls. The greatest lengthening was experienced by stream 1980, whose length increased by ~3.5 km between 1957 and 1980. The new stream reaches exposed in each tributary watershed were at a much higher gradient, particularly at the head of the fjord where the fjord walls are steepest. This lengthening and increased gradient of the new channel reaches caused dramatic shifts in the planimetric form of the streams, causing upstream braided reaches to transition into single-thread morphologies.

Channel shifts and abandonment were also seen in multiple watersheds that had the ability to laterally adjust to a lowering of base-level. Stream 1967 shifted 90 degrees at its outlet from an old channel that paralleled the modern-day shoreline to one that dropped straight into the fjord. The remnants of this can still be seen as a vegetated channel perpendicular to the current stream ~0.5km upstream from the fan-delta apex (figure 3-4). In watershed 1988, terraces and abandoned channels can be seen high above the modern-day channel bed, suggesting incision

was particularly rapid in this basin. Streams that had incised into large canyons, including streams 1983, 1984, 1985, and 1987, responded to base-level fall vertically as the canyon walls restricted lateral movement.

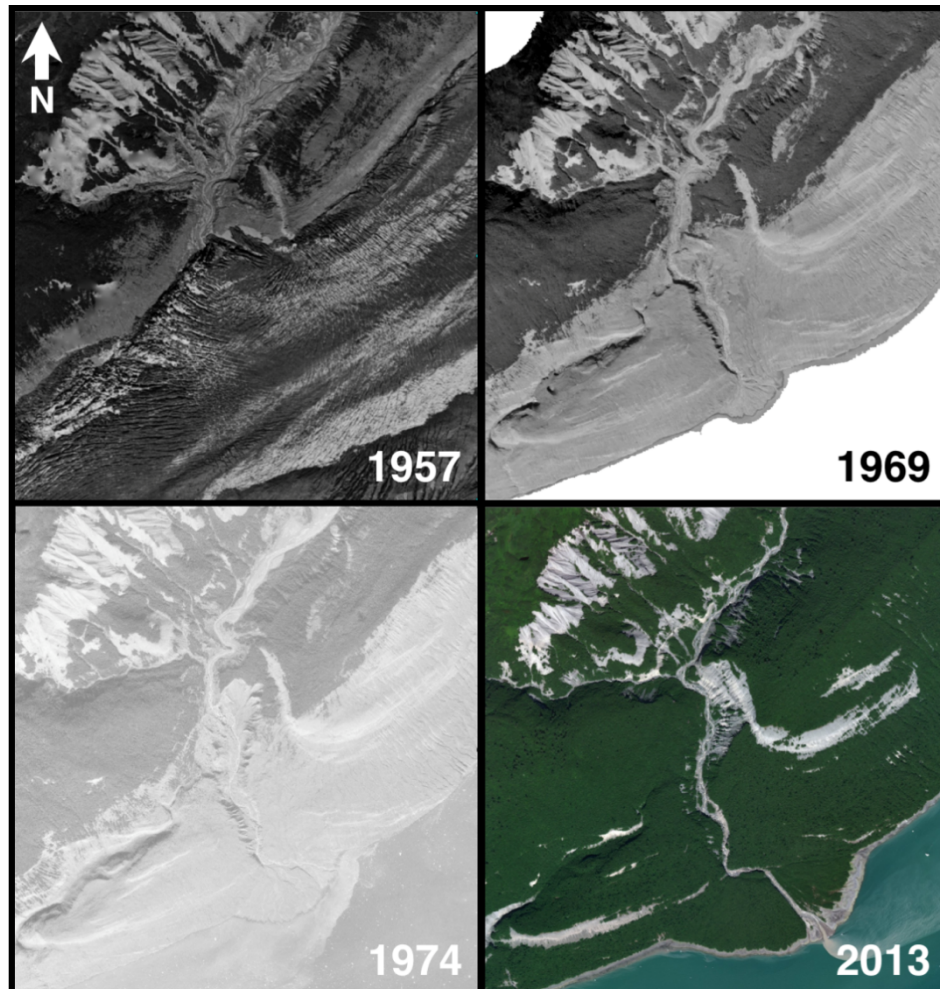


Figure 3-4. The outlet of watershed 1967 in the years 1957, 1969, 1974, and 2013. The main trunk of Tyndall Glacier is present in the first panel (1957) and completely gone in the 1969 panel. A large exposed face of loose Yakataga bedrock can be seen in the top left corner of all panels and remains similarly vegetated across all years, suggesting this steep face is likely a consistent sediment source for the stream. The previous, ice-marginal channel can be seen traversing the bedrock wall in parallel to and high above the modern-day shoreline. The last panel shows a highly vegetated fan-delta 1967 with one active main channel.

Quick falls in base-level often lead to the formation of knickpoints along the lower reaches of a stream profile (Schumm, 1993) and this was consistently observed in six of the eight tributary streams (figure 3-5). For stream 1967, a knickpoint over 70 m above the 2016 channel bed formed between 1957 and 1969. It was quickly eroded with no evidence of continued

migration upstream, suggesting it was primarily composed of non-cohesive, easily erodible sediment. Knickpoints were still prominent features in the 2016 profiles of streams 1973, 1980, 1985, and 1988 and they had migrated significant distances upstream. For instance, the knickpoint of stream 1988 had migrated 2.2 km upstream between 1957 and 2016 at a rate of almost 50 m yr^{-1} . The persistence of these knickpoints in the longitudinal profiles of these streams along with their rapid rate of migration suggests that these knickpoints once eroded through non-cohesive lake sediment and have perhaps encountered tougher material or even bedrock that has slowed their progression upstream. No clear knickpoints were seen in streams 1983, 1984, and 1987.

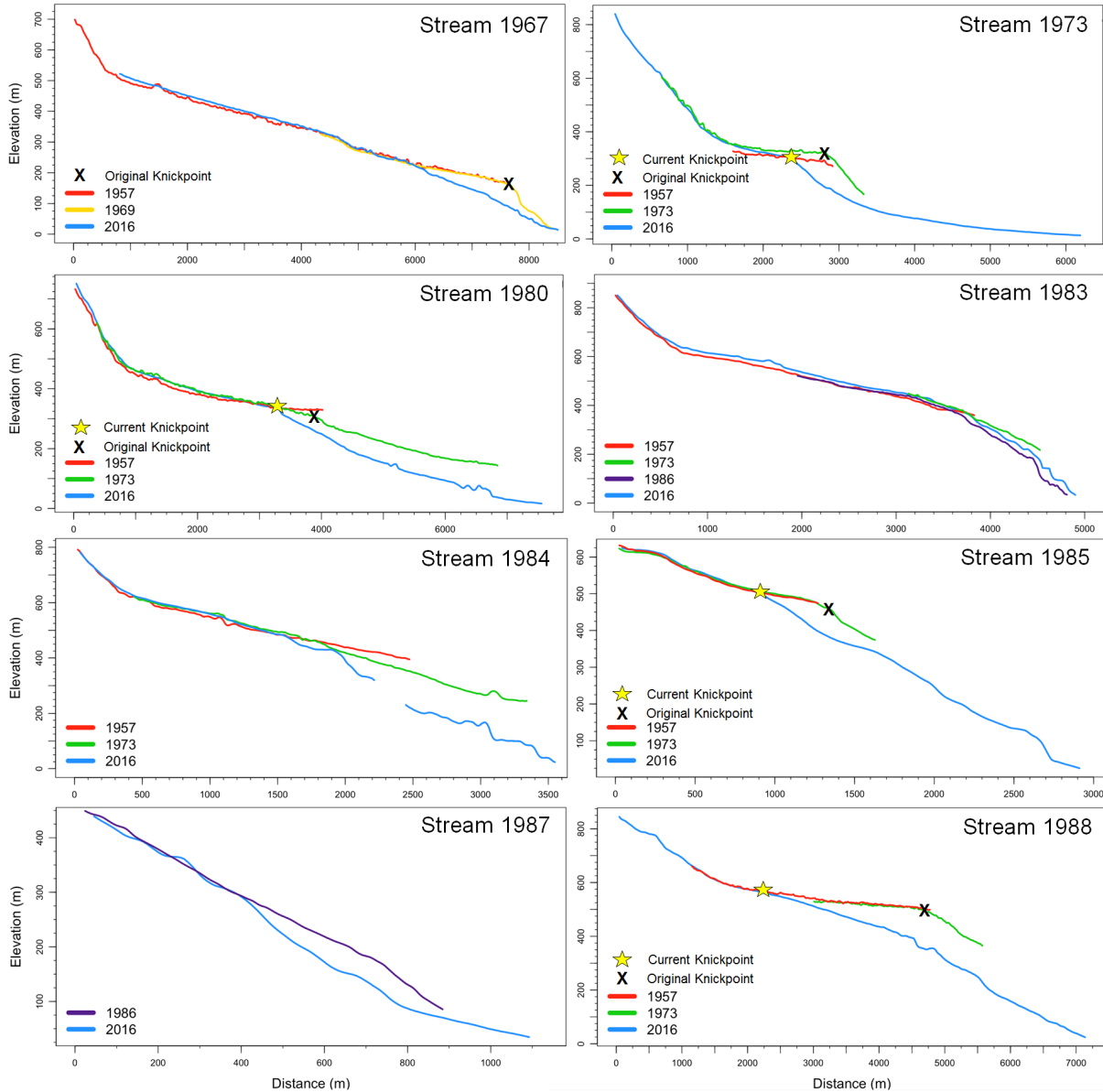


Figure 3-5. Longitudinal profiles for each stream with black x marking the original knickpoints that developed following base-level fall.

3.2.3 Error in Volume Models

A probability density function (PDF) of the volumes of the fan-deltas in Taan Fjord in 2016 produced 100,000 volume estimates for each fan-delta within the realm of possible errors associated with the model input parameters (figure 3-6). These PDFs were generally negligibly positively skewed towards a larger volume estimate, with the exception of the output for

watershed 1983 which had a pronounced positive skew. To account for this skew, the median value for each distribution was taken as the volume in each of the fan-deltas.

The 25th and 75th percentiles were used as the standard error of the volume estimates. Results can be found in table 3-3. When obtaining sediment yields and erosion rates through time for each watershed, the proportion of volumes that fell between the 25th and 75th percentiles in the original calculation was applied for timescales before 2016 to obtain an estimate of error.

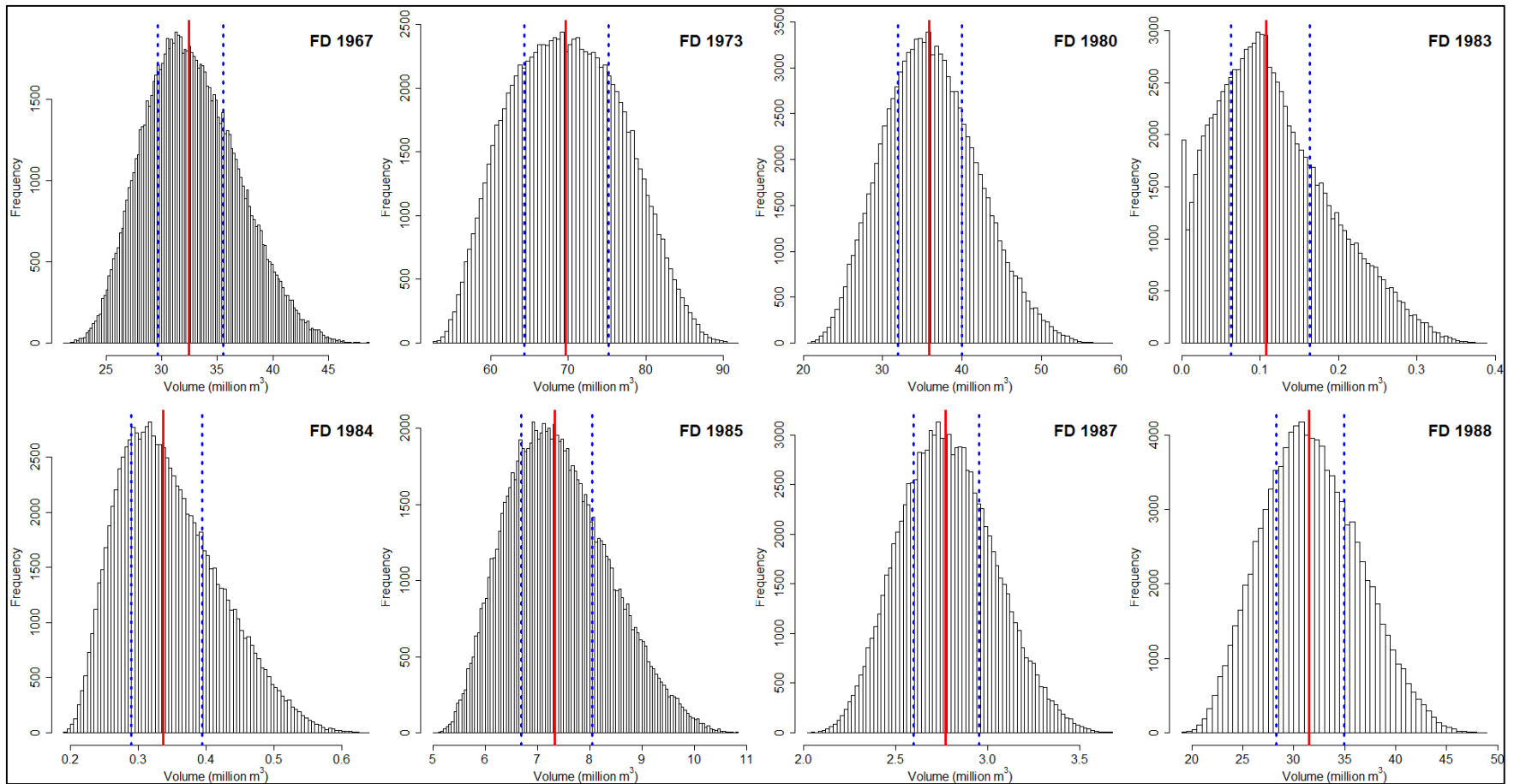


Figure 3-6. Monte Carlo volume distributions for each fan-delta in Taan Fjord. Red lines indicate the median volume and the dotted blue lines signify one standard error.

3.2.4 Sediment Yield and Basin-Averaged Erosion Rates

The tributary valleys are a major contributor of sediment to the fan-deltas in Taan Fjord (figure 3-7; table 3-3). In total, the combined volume of paraglacial sediment contained in the fan-deltas of Taan Fjord in 2014 (pre-tsunami) was 165.7 ± 16.0 million m^3 (table 3-3). The greatest amount of sediment accumulated in fan-delta 1973 at ~ 60 million m^3 . Fan-delta 1983 contained the least sediment at only ~ 0.11 million m^3 .

The pre-tsunami volume was chosen to capture the volume that accumulated in the fans before the 2015 landslide event. However, the method used to obtain the 2014 volumes involved the use of 2016 (post-tsunami) fan-delta geometries due to limitations in available data. Thus, the effects of the tsunami on fan-delta geometry likely carried through all the volumetric estimates in this study, however it is unknown how large of an impact this had on the results. We assume the impacts are greatest near the head of the fjord where the tsunami runup was highest (192 m) and less on more distal fan-deltas near the fjord entrance. Further discussion on the impact of the tsunami on fan-delta geometry is addressed in section 4.4.

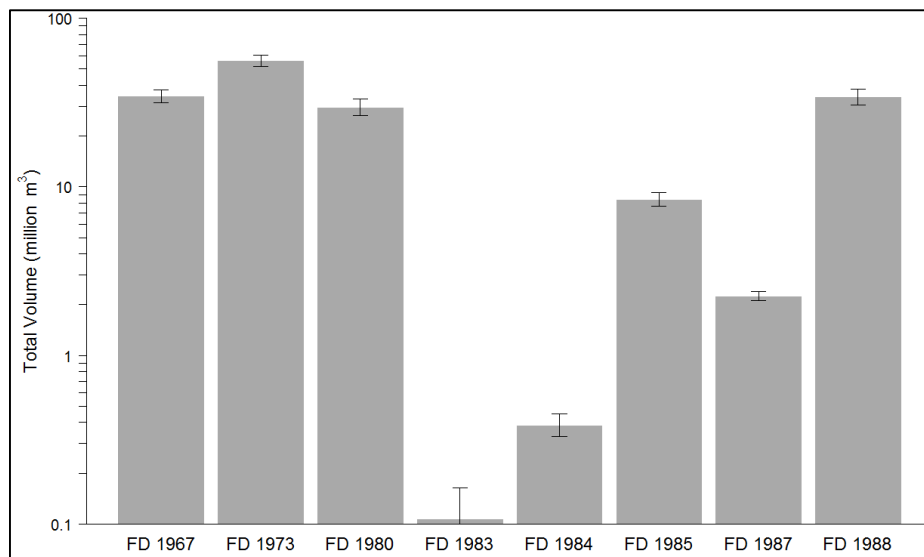


Figure 3-7. Total volume in the fan-deltas of Taan Fjord in 2014 (pre-tsunami) on a logarithmic scale. Their dates correspond to the first year of fan-delta formation and thus the oldest fan-deltas are on the left of the graph and the youngest are on the right.

The greatest volume of sediment appeared to be in the oldest fan-deltas; however, the youngest fan-delta (fan-delta 1988) had a volume comparable with the three oldest fan-deltas. Hence, there was no clear relationship observed between time of fan-delta formation and total volume stored. There were likely other variables influencing accumulation rates on the fan-deltas of Taan Fjord that were unrelated to fan-delta age, including sediment availability, the presence and activity of faults, and bedrock lithology in the watersheds.

	1967	1973	1980	1983	1984	1985	1987	1988
Total 2014 Volume (million m³)	34.4 ± 3.3	56.3 ± 4.4	29.7 ± 3.5	0.11 ± 0.06	0.4 ± 0.07	8.4 ± 0.8	2.2 ± 0.1	34.2 ± 3.8
Avg. Sed. Yield (million m³yr⁻¹) 1969-2014	1.3 ± 0.1	0.47 ± 0.04	1.4 ± 0.02	0.003 ± 0.001	0.012 ± 0.002	0.23 ± 0.02	0.071 ± 0.005	1.0 ± 0.1
Min. Sed. Yield (million m ³ yr ⁻¹)	0.045 ± 0.004	0.114 ± 0.009	0.49 ± 0.06	---	0.0034 ± 0.0006	0.0877 ± 0.009	0.0327 ± 0.002	0.41 ± 0.04
Max. Sed. Yield (million m ³ yr ⁻¹)	4.2 ± 0.4	2.0 ± 0.2	4.8 ± 0.6	---	0.029 ± 0.005	0.65 ± 0.06	0.16 ± 0.01	3.7 ± 0.4
Avg. Basin Avg. Erosion Rate (mm yr⁻¹) 1969-2014	45.0 ± 4.3	27.0 ± 2.1	39.0 ± 4.6	0.2 ± 0.1	1.5 ± 0.3	100.5 ± 9.9	53.6 ± 3.5	58.9 ± 6.6
Min. Basin Avg. Erosion Rate (mm yr ⁻¹)	1.6 ± 0.1	6.5 ± 0.5	13.9 ± 1.6	---	0.4 ± 0.07	38.2 ± 3.8	24.7 ± 1.6	22.8 ± 2.6
Max. Basin Avg Erosion Rate (mm yr ⁻¹)	145.5 ± 13.8	111.7 ± 8.8	137.2 ± 16.1	---	3.7 ± 0.6	282.3 ± 27.9	119.8 ± 7.8	208.6 ± 23.3

Table 3-3. Tabulated results for total fan-delta volume, sediment yield, and basin averaged erosion rate including minimum and maximum yields and erosion rates.

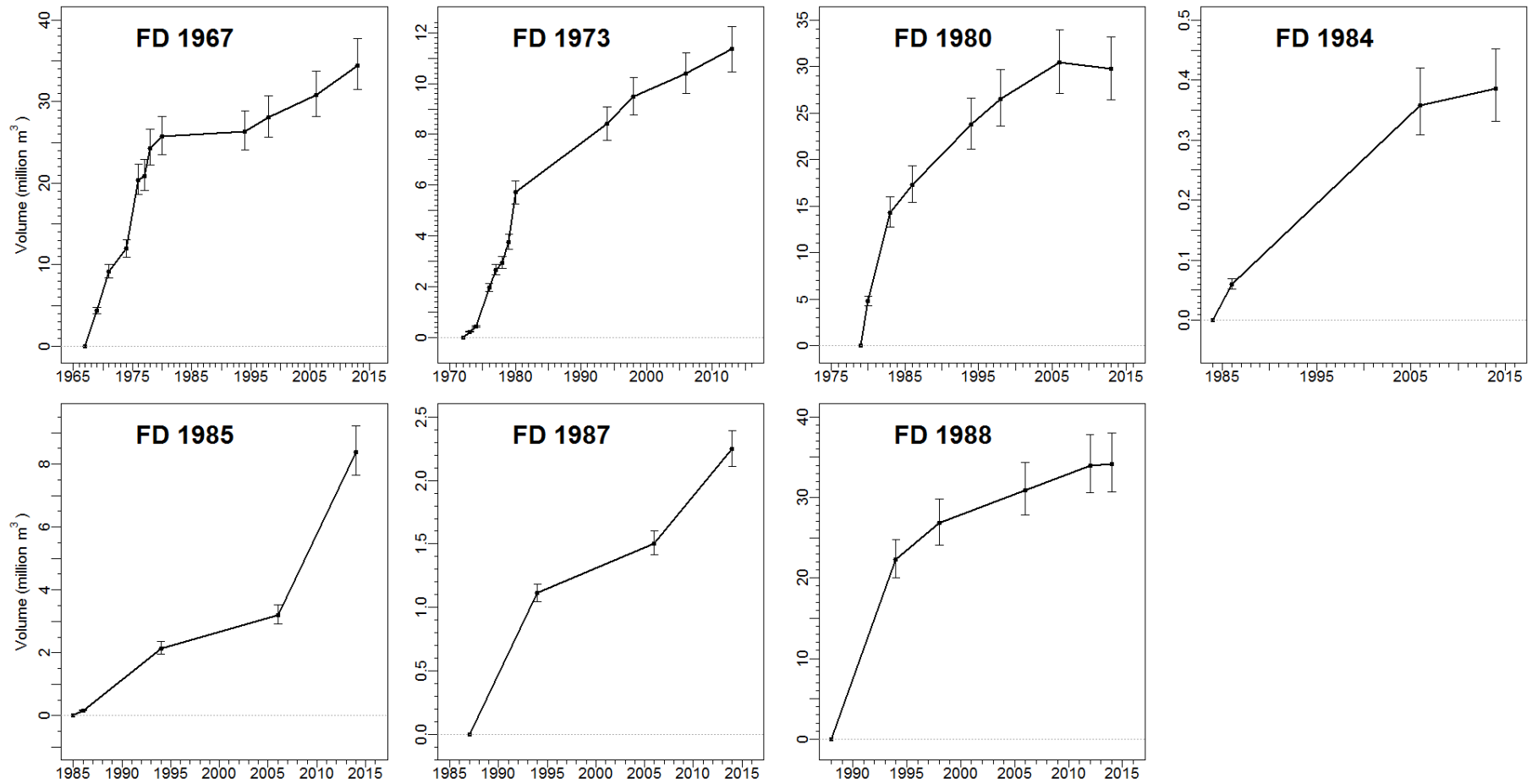


Figure 3-8. Volume growth of each fan-delta since fan-delta progradation began. Most fan-deltas follow the trend of rapid growth at the onset of fan-delta formation, with a tapering in the volume added over time. Only watersheds 1985 and 1987 seem to not follow this trend, as they had a slight uptick in growth since 2006.

Sediment yields and basin-averaged erosion rates were determined for years before the 2015 landslide event for all of the watersheds to gain an understanding of the rate of relaxation in each before the fan-deltas were altered by the tsunami. The combined average sediment yield of all the tributary valleys was 4.3 ± 0.3 million m^3yr^{-1} . This figure was obtained by summing the average yields for each tributary valley. The three watersheds at the entrance of the fjord had the highest yields, but again the youngest watershed at the head of the fjord had a comparable sediment yield, suggesting other possible lurking variables were impacting sediment yields, such as bedrock lithology and structure.

The three watersheds at the head of the fjord (1985, 1987, and 1988) appeared to be the most erosive (figure 3-9b). Watershed 1985 had an erosion rate that was an order of magnitude higher than all other basins at 100 ± 10 mm yr^{-1} . The tributary valleys combined had an average basin-averaged erosion rate of 36.0 ± 5.7 mm yr^{-1} . This was found by summing all of the average tributary sediment yields, multiplying by the density ratio of saturated fan sediment (1600 kg m^{-3}) to the Yakataga bedrock (2350 kg m^{-3}), and then finally dividing by total area of all the watersheds.

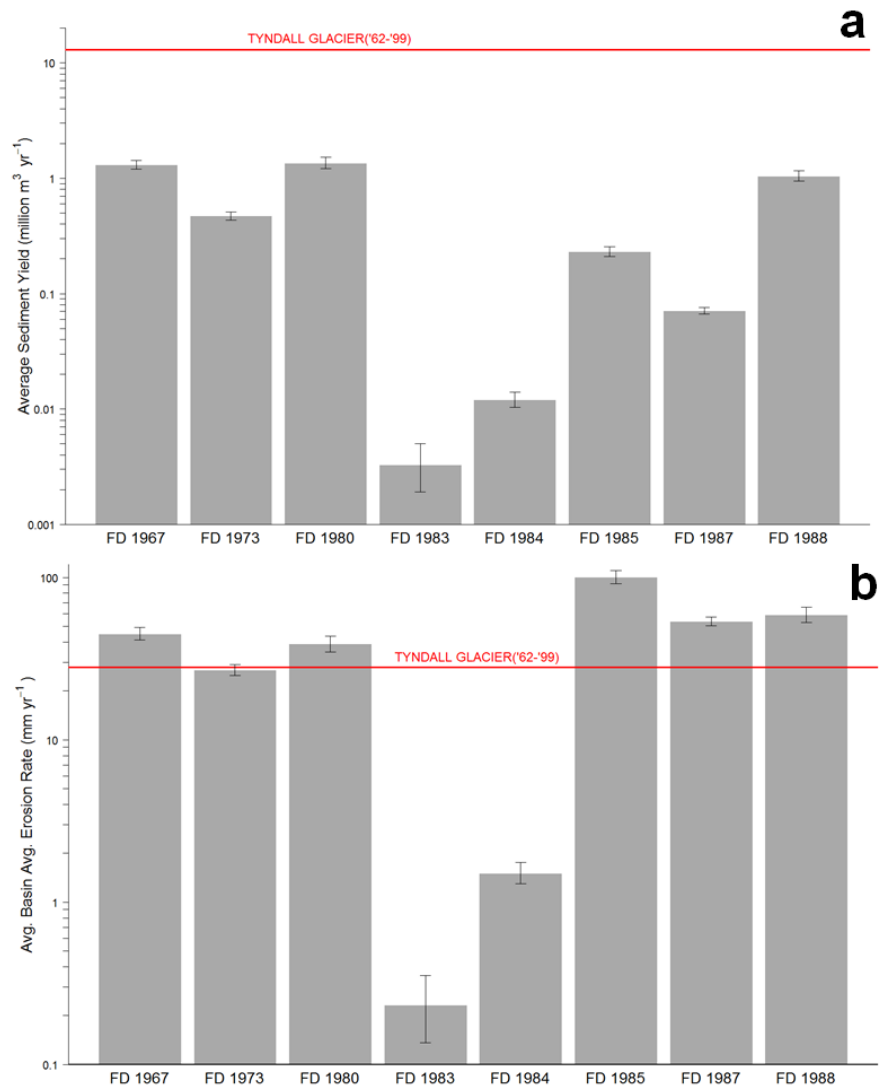


Figure 3-9. Average sediment yields (a) and basin-averaged erosion rates (b) for all tributary basins on a logarithmic scale. The sediment yield and erosion rate of Tyndall Glacier between 1962 and 1999 are labelled in red and were 13.0 ± 0.2 million $m^3 yr^{-1}$ and 28 ± 5 $mm yr^{-1}$ respectively (Koppes and Hallet, 2006).

Sediment yields and basin-averaged erosion rates of the tributary basins shared the same general trend. Within the first decade that immediately followed Tyndall Glacier retreating past their outlets, there was a peak in sediment yield and hence erosion rates in all watersheds (figures 3-10, 3-11). Yields then proceeded to decrease over time, with the exception of watersheds 1985 and 1987 which both experienced a jump in yields and erosion rates between 2006 and 2014 (figures 3-10, 3-11).

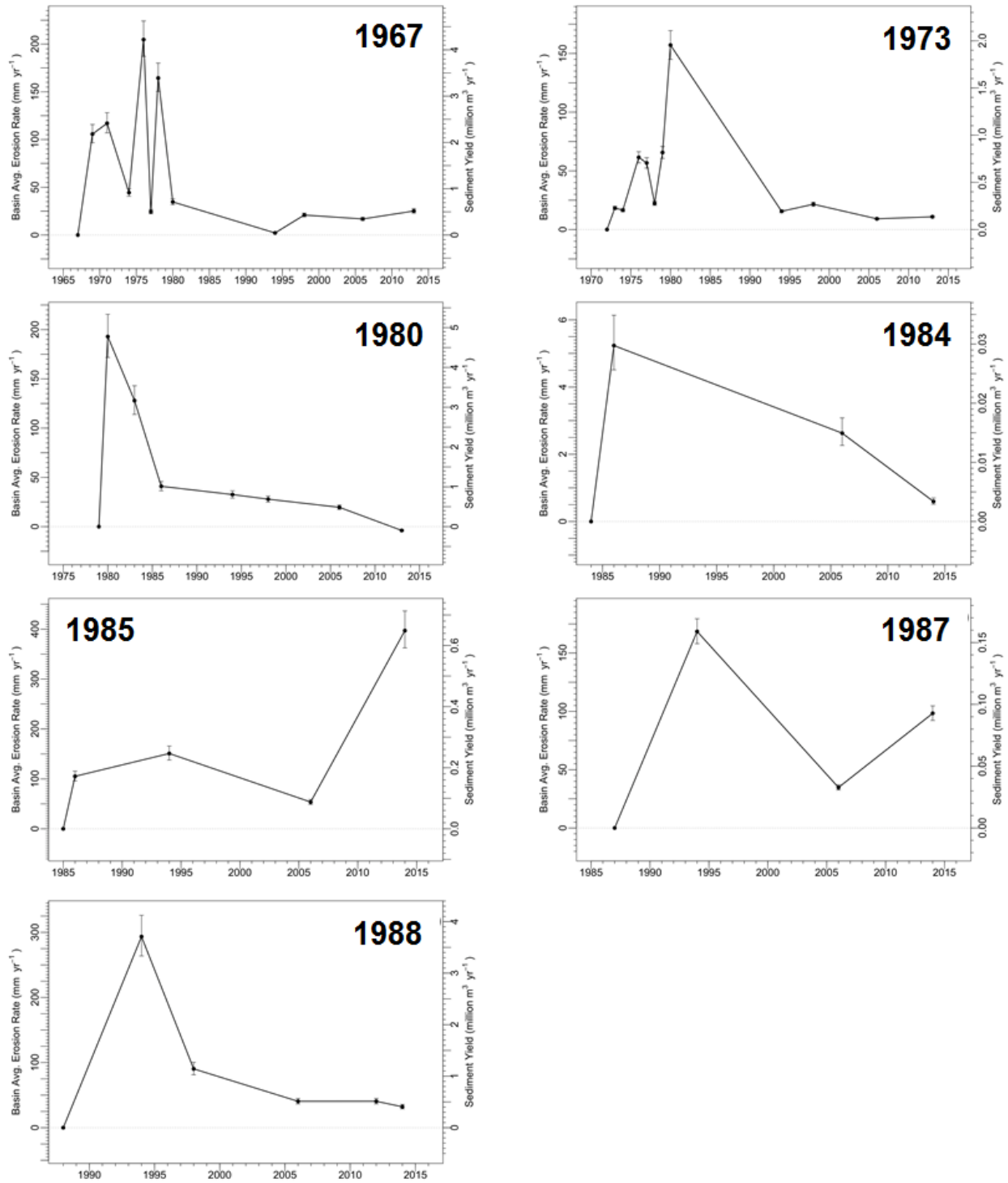


Figure 3-10. Basin-averaged erosion rates (left y-axis) and sediment yields (right y-axis) of the eight tributary basins of Taan Fjord.

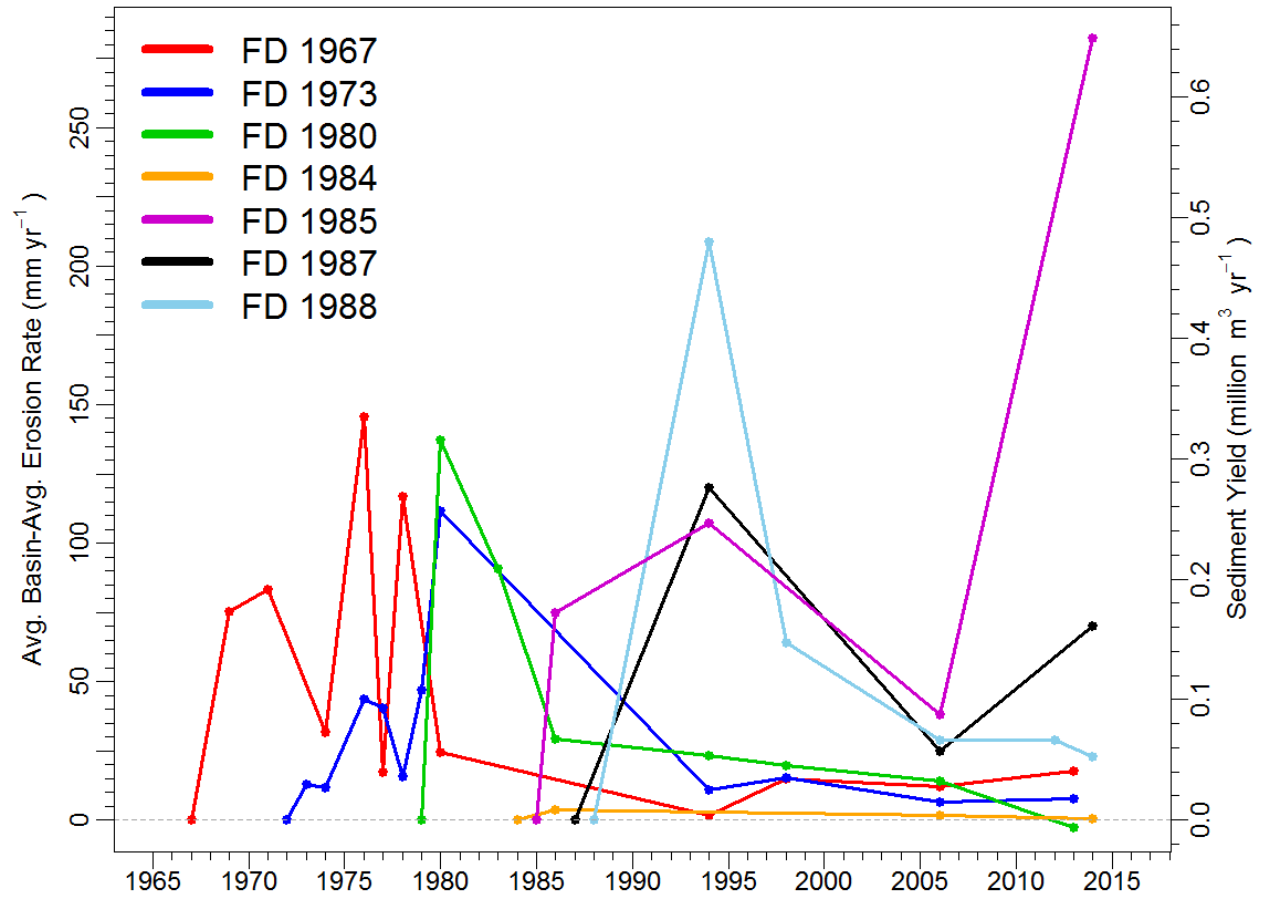


Figure 3-11. Basin-averaged erosion rates (left y-axis) and sediment yields (right y-axis) of the eight tributary basins of Taan Fjord plotted together at the same scale. Of note are the jumps in erosion rates and yields between 2006 and 2014 for watersheds 1985 and 1987.

Chapter 4: Discussion

The tributary basins of Taan Fjord have all responded rapidly to the thinning and retreat of Tyndall Glacier since it first separated from the main trunk glacier in Icy Bay in 1961.

Thinning of the glacier surface and eventual loss of the ice blocking their outlets meant the tributary streams experienced an average base level fall of almost 400 m with even greater drops (>500 m) observed for tributaries at the head of the fjord. Base-level fall in Taan Fjord was extreme in terms of the rapidity and total amount of fall, and extreme base-level change has the potential to trigger rejuvenation, or adjustment in slope and morphology, of the entire drainage network (Schumm, 1993).

Rapid base-level fall releases a quick but major pulse of sediment to a system (Schumm, 1993) followed by a decline to some sediment yield that is higher than the previous “normal” (Schumm and Rea, 1995). This increase in sediment yield can be attributed to increased physical erosion rates following the base-level drop (Schumm and Rea, 1995). Almost all of the tributary watersheds in Taan Fjord follow this trend with the exception of watersheds with other extenuating factors such as active thrust faulting and sediment availability influencing yield. Despite these additional factors, base-level fall triggered by glacier retreat had immediate effects on the lower reaches of all eight tributaries and was the driving mechanism behind rapid geomorphic change, increased sediment yields, and higher basin-averaged erosion rates in the tributary watersheds of Taan Fjord.

4.1 Geomorphic Evolution

In 1957, Tyndall Glacier dammed the outlets of all eight tributary basins and ice-marginal lakes were present in all watersheds with the exception of watershed 1987, which was almost completely covered in ice. When these lakes drained following the thinning of the glacier

surface, ice-marginal outwash deposits, sometimes quite large, were left exposed and prone to rapid incision by the tributary streams. Therefore, these were the first sediments to be flushed from the watersheds and were the main sources of sediment for some basins for several decades. This was particularly pronounced in watershed 1988, where in addition to ice-marginal outwash sediment, stored colluvium, till from Tyndall Glacier, and glaciofluvial sediment in the valley have been excavated by the stream (Meigs et al., 2006; Koppes and Hallet, 2006). It was this quick flushing of large glaciolacustrine sediment in combination with rapid incision through till and colluvium that led to a rapid and large accumulation of sediment on fan-delta 1988. This is reflected in watershed 1988's very high yields and erosion rates, despite this watershed being the most recently exposed.

The incision of the tributary streams deepened existing canyons and created new ones in most of the watersheds with the most pronounced incision occurring downstream of knickpoints, where they existed. These knickpoints formed cascades along lower reaches of most of the streams. Stranded terraces with abandoned stream channels on their surfaces were also observed in multiple watersheds, further verifying the rapidity at which incision took place.

The knickpoints that formed along some of the tributary streams all developed at the margin of ice-marginal lake deposits. It's understood that if a knickpoint is established in non-cohesive, easily erodible sediment (such as loose lake-bed material), it will likely be quickly obliterated (Brush and Wolman, 1960). This behavior was exhibited in watersheds 1967 and 1985, where knickpoints visible in earlier profiles were not present in any reach of the 2016 profiles. In the case of stream 1967, the knickpoint near its outlet was 70 m above the 2016 channel suggesting a quick redistribution of a large volume of material from the channel to the fan-delta. If a knickpoint is composed of more resistant, cohesive material, it can migrate a

significant distance upstream (Brush and Wolman, 1960). The knickpoints along streams 1973, 1980, and 1988 tended towards this behavior and are still visible in the 2016 profiles. This was likely due to the knickpoint encountering more resistant bedrock in the watershed after the lake sediment was exhausted.

Those profiles that contain knickpoints show little to no change in the reaches above the knickpoint. Base-level changes typically have the greatest impact on downstream reaches of a stream and propagate those changes throughout the drainage basin with diminishing effect (Blum and Törnqvist, 2000; Holbrook et al., 2010). In other words, the consequences of the base-level fall have simply not yet reached the headwaters of most of the tributaries in Taan Fjord. However, theory suggests that in pursuit of equilibrium, the streams will continue to incise and their knickpoints will continue to migrate upstream until they achieve a smooth, concave profile. Thus, this paraglacial signal will be preserved in the longitudinal profiles of the tributary streams of Taan Fjord for decades or perhaps longer if a knickpoint migrates into particularly resistant material. This may arise in the headwaters of watersheds 1987 and 1988 where lithologic boundaries exist between the Yakataga, Poul Creek, and Kulthieth formations.

The tributary streams of Taan Fjord also visibly changed in planimetric form. In 1957, streams 1967, 1973, 1980, and 1988 exhibited a braided morphology, suggesting that the streambeds were relatively low gradient and the streams had an ample sediment supply. After the glacier thinned and base-level fell, the streams experienced a dramatic lengthening of their channels, sometimes exceeding double their original length. All the basins are non-glaciated and thus rely on snowmelt, rainfall and groundwater for their flow, which likely remained relatively consistent since 1957. This meant that the streams suddenly needed to transport roughly the same

amount of sediment over double their original length, and so channel form in their headwaters transitioned from a braided to single-thread morphology.

4.1.1 Geomorphic Evolution: Watershed 1967

Stream 1967 is an excellent example of how quickly paraglacial systems can rework sediment and alter the landscape. Fan-delta 1967 was the first to be exposed to Taan Fjord and experienced overall growth that confirms what is believed about the evolution of paraglacial fans: rapid growth occurs at the beginning of the paraglacial period and wanes through time (Ballantyne, 2002; Church and Ryder, 1972; Owen and Sharma, 1998; Ryder, 1971). The rate of growth of fan-delta 1967 spiked in the mid to late 1970s (figure 4-1) at which time the stream was actively eroding large features at its outlet. In figure 4-1, a wedge of sediment near the outlet of stream 1967 can be seen in 1974 but not in 1976, indicating that in just two years, the stream had eroded this feature in order to access a straighter path to the fjord.

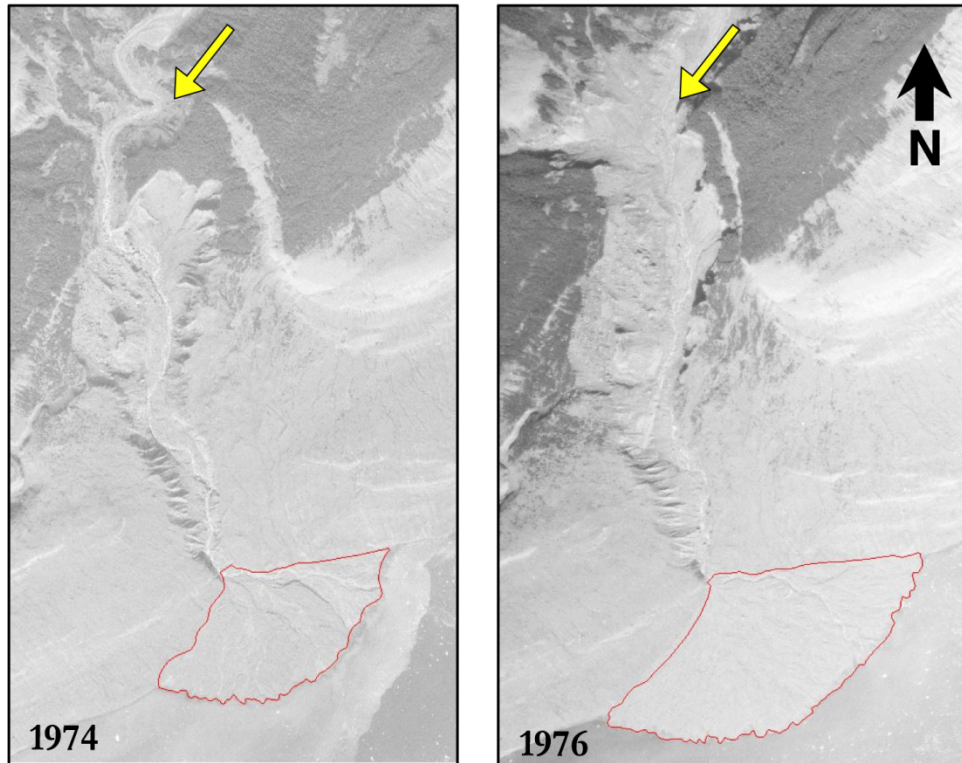


Figure 4-1. FD 1967 between 1974 and 1976 in which it experienced rapid growth. The yellow arrow points to an outcrop of sediment that was present in 1974 but had been completely eroded by the stream by 1976. It is suspected that the displacement of this sediment wedge contributed to the rapid growth of the fan-delta during this time. Also of note is the change in area of the fan-delta.

4.2 Sediment Yields and Erosion Rates

The rapid geomorphic changes described previously had a dramatic impact on sediment yields and basin-averaged erosion rates of the tributary basins. The most dramatic changes were seen in those watersheds with an abundance of stored sediment in the forms of ice-marginal outwash sediment and/or till and colluvium deposits. This was most pronounced in watershed 1988 where the stream tapped not only outwash sediment, but also previous moraines deposited by a tongue of ice that Tyndall Glacier pushed into the watershed (Meigs et al., 2006).

Other watersheds were generally sediment starved as they had no significant storage of sediment and instead relied primarily on bedrock erosion. Perhaps the most interesting example of this is watershed 1983. Fan-delta 1983 is hardly discernible above the fjord's surface at high

tide, however a steep canyon at its outlet hints at its existence (figure 4-2). A fan-delta does exist subaqueously at its outlet but it is the smallest of all the fan-deltas. A simple story of incision following significant base-level fall doesn't adequately explain this fan-delta's small size yet highly dissected outlet.

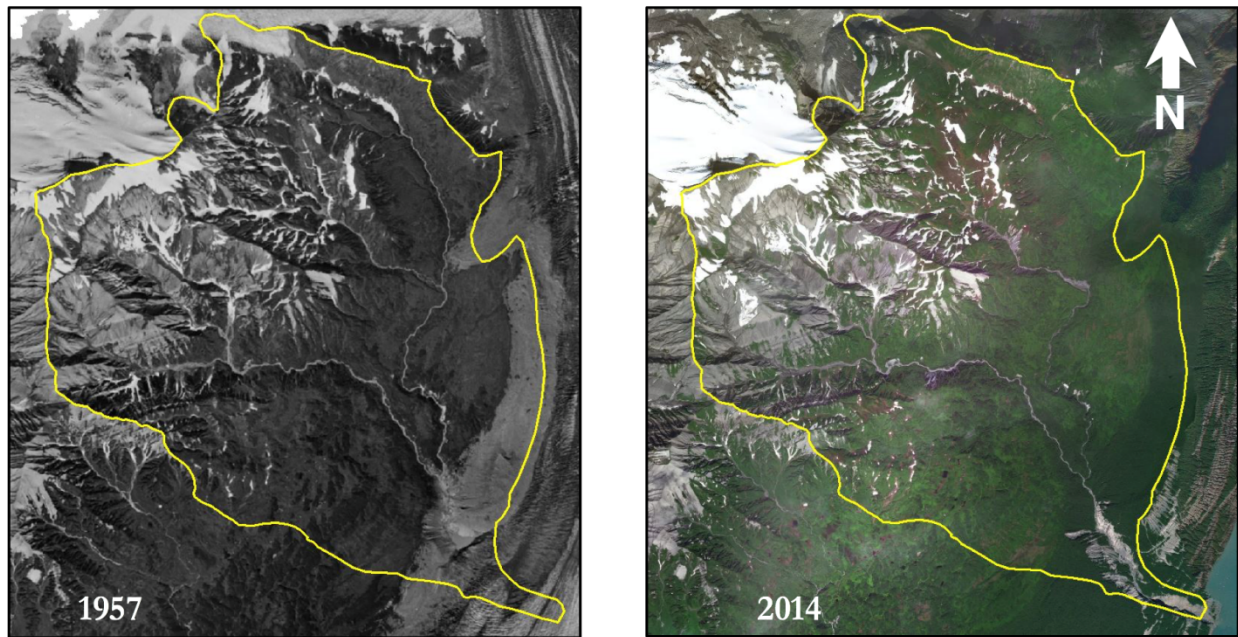


Figure 4-2. Watershed 1983 in 1957 (left) and 2014 (right). Changes in sources of flow can be seen in the northernmost valley where a tongue of glacier ice once supplied flow to stream 1983 but is no longer present. The canyon at the outlet of the stream can be seen in 1957 and is partially filled with an ice-marginal lake.

We believe much of watershed 1983 has remained unchanged since 1957 and that changes in the headwaters of the watershed may have actually decreased the amount of sediment and flow passing through the stream. In 1957, a lobe of ice stemming from Daisy Glacier can be seen contributing flow to stream 1983, but this lobe of ice was completely gone by 1973. This effectively cut off sediment and flow from that region of the watershed (figure 4-2).

The start of the deep canyon at the outlet of watershed 1983 is visible in 1957 and appears to have already been developed. The stream was actively flowing into an ice-marginal lake at the start of the canyon at this time (figure 4-2). This implies that dissection of the canyon did not exclusively follow glacier retreat but rather could have been formed subglacially when

Tyndall Glacier still occupied the outlet. When ice retreated, the stream simply occupied the existing canyon. In profile, the only real changes to the stream are in the canyon reaches, however the vertical changes are negligible.

Lastly, the fjord wall underlying fan-delta 1983 is the steepest of all the fjord slopes. The subaqueous slope of the fan-delta surface is also the steepest. This is likely an indication that underlying fan-geometry is a limiting factor on fan-delta size, and that the steep front of fan-delta 1983 might have difficulty retaining sediment on its surface at such a high angle of repose. All of these observations suggest that the substrate being eroded (bedrock or loose sediment), pre-existing stream morphology and underlying fan-delta geometry all play a role in determining the total sediment yield for each tributary basin.

4.2.1 Lithology and Bedrock Structure

The high rates of erosion in the upper watersheds of Taan Fjord, particularly of watersheds 1985, 1987 and 1988, cannot be reconciled without acknowledgement of the lithology and tectonic setting of Taan Fjord (figure 4-3). The watersheds are mostly composed of Yakataga Formation bedrock, however a small region of the Poul Creek Formation is present in watershed 1988 and in the headwaters of watershed 1985. Watershed 1988 also contains some of the Kulthieth Formation on its northern edge (Meigs et al., 2006).

This complex geology at the head of the fjord is due to the presence of the Chaix-Hills thrust fault that bisects the fjord in this location (figure 4-3). In this region, the fault has a right-lateral slip rate of $8.3 \pm 8.7 \text{ mm yr}^{-1}$ and reverse slip rate of $14.3 \pm 1.8 \text{ mm yr}^{-1}$ (Elliot et al., 2013). The fault runs through significant portions of the 1985, 1987 and 1988 watersheds. In fact, watersheds 1985 and 1988 appear to exist on the two splayed arms of the Chaix-Hills fault. In addition to the slip rates of the fault, the St. Elias Orogen experiences $\sim 33 \text{ mm yr}^{-1}$ of

convergence, which is extremely high (Elliot et al. ,2013). These high strain rates lead to uplift rates in the region that rival that of the western Himalaya (Bruhn et al., 2004; Enkleman et al., 2009).

The presence and activity of this fault in addition to the patchwork of exposed bedrock likely contribute to the high basin-averaged erosion rates calculated for the watersheds at the head of the fjord. Thrust faulting has been documented to increase erosion rates in the immediate vicinity of thrust faults (Dadson et al., 2003; Tucker and Slinger, 1996), further suggesting that the high erosion rates in the watersheds that intersect the Chaix-Hills thrust fault are likely due in part to movement along the fault. Additionally, the lithologies present along this fault are known to be deformed (Kulthieth and Poul Creek) and relatively weak (Kulthieth, Poul Creek and Yakataga), thereby increasing erosion rates at the fault boundary (Tucker and Slinger, 1996).

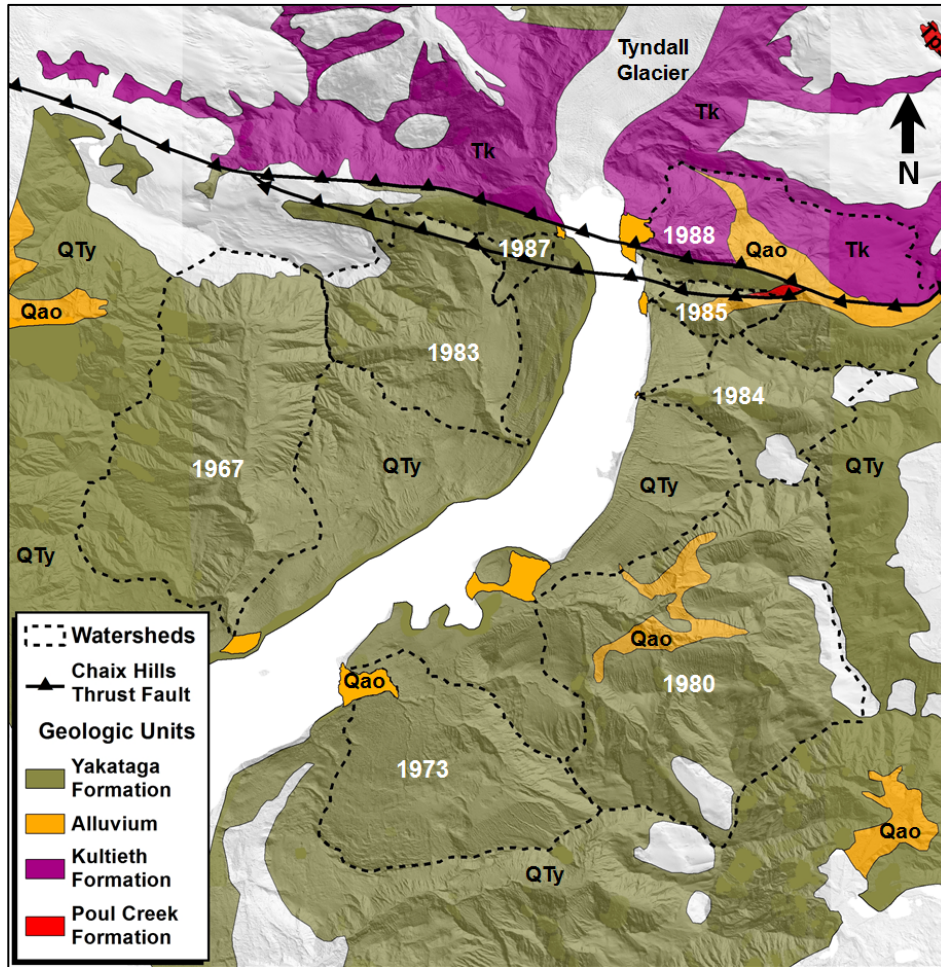


Figure 4-3. Map detailing the geologic units and active faulting in Taan Fjord with watersheds outlined in light blue. Watersheds 1985 and 1988 are directly bisected by the Chaix-Hills thrust fault on the western side of the fjord, whereas watershed 1987 and a small section of watershed 1983 are in direct contact with the fault on the eastern side of the fjord.

4.2.2 Variables Driving Change

Collectively, the rate at which the tributaries eroded their watersheds following the retreat of Tyndall Glacier was mostly a function of the type of material being eroded in the watershed (bedrock or loose sediment). A basin with ample sediment stores in the form of ice-marginal outwash deposits or till tended to produce larger fan-deltas and have higher yields than those watersheds that relied primarily on bedrock erosion as a source of sediment.

The time since ice retreated past the outlets of the tributary basins was also a significant factor in the total volume of sediment present within each fan-delta. Fan-deltas at the entrance to

the fjord were generally larger than those at the head of the fjord, with the exception of watershed 1988. However as previously mentioned, we believe the size of fan-delta 1988 was strongly conditioned by the presence of large sediment deposits in its watershed.

Lastly, the unique geology at the head of the fjord boosted yields and erosion rates in basins where thrust faulting is active. Interestingly, watershed size wasn't an obvious predictor of fan-delta size or average yield, as some of the smallest basins turned out to be the most erosive, and large basins, such as watershed 1983, hardly contributed any sediment to the fjord at all. For these reasons, we believe the main variables driving sediment yields in the tributary basins of Taan Fjord are paraglacial sediment availability, time since outlet exposure, and the lithology and structure of the bedrock.

4.2.3 Assumptions

Basin-averaged erosion rates were determined by using the densities of the primary bedrock in Taan Fjord and of the saturated fan-delta sediments. The bulk density used for the fan-deltas (1600 kg m^{-3}) was chosen based on similar studies done on fan-deltas in British Columbia (Pelpoa and Hickin, 2004; Tunnicliffe et al., 2012). Pelpoa and Hickin (2004) determined the average bulk density of the Fitzsimmons Creek fan-delta, a fan-delta located in the Coast Mountains of British Columbia. To determine a density of the total fan-delta sediment package, they used cube sampling techniques of near-surface sediments, previous studies on the fan-deltas of the Lillooet and Squamish rivers (Gilbert, 1975; Hickin, 1989), as well as USGS guidelines for the density subaqueous sands and gravels (Vanoni, 1975). In addition to being geographically close to Southeast Alaska, large-scale basins in British Columbia remain in a phase of paraglacial relaxation (Church and Slaymaker, 1989), drawing parallels between the fan-deltas found in the Coast Mountains of BC and those found in Southeast Alaska.

Density of the primary bedrock in Taan Fjord, the Yakataga Formation was assumed to be similar to those in the Cook Inlet region (Haeussler et al., in press; Mankemthong et al. 2013; Saltus et al. 2016). Additionally, watershed 1988 encompasses the Yakataga, Kultieth, and Poul Creek Formations and watershed 1985 also contains a small amount of Poul Creek Formation in its headwaters. The density for the Kultieth and Poul Creek Formation range from 2700 – 2790 kg m⁻³ (Koppes and Hallet, 2006; Plafker et al., 1994), however for this study, only the assumed density for the Yakataga Formation (2350 kg m⁻³) was used.

Variations in these assumed densities would have no effect on the total volumes and sediment yields of the tributary basins as they are not needed in the calculation of these estimates. They would have a small effect on the basin-averaged erosion rates and be well within an order of magnitude of the estimates found in this study.

It should also be noted that sediment yields and erosion rates were influenced by data availability. Aerial photos of the fjord were abundant from the early 1970's through the 1980's, however little imagery was available for the fjord between 1986 and 2000. Yields and erosion rates are time-averaged figures and thus, when averaging over longer timescales due to the lack of available data, signals may be muted or lost. For example, had a sudden peak of sedimentation occurred on fan-delta 1984 in 1991, its signal might have been lost because its yield and erosion rates were averaged between 1986 and 2000.

4.4 October 2015 Landslide & Tsunami

The 2015 event had significant impacts on the surfaces of the fan-deltas in Taan Fjord, particularly those closest to the landslide at the head of the fjord. The total fan-delta volumes, sediment yields, and basin-averaged erosion rates found in this study all rested on the configurations of the fan-deltas after the tsunami had occurred. Any effects of the 2015 event on

the variables used as the main model parameters could have had an impact on the fan-delta volume estimates and subsequently the sediment yield and erosion rate estimates. In order to constrain our estimates, we analyzed the likely impacts of the tsunami on the fan-deltas of Taan Fjord.

As reported by Bloom et al. (2017), the landslide and tsunami impacted fan-deltas 1988, 1987, and 1985 the most as they were the closest to the landslide. The fronts of fan-deltas 1988 and 1985 were dissected during the event, creating 5 – 6 m vertical scarps where the fan surfaces used to enter the water at a gentle gradient (Bloom et al., 2017). Additionally, it was suggested that subaqueous delta-front failures also occurred during the event due to the undercutting of the toes of deltas 1988 and 1985 (Bloom et al., 2017).

These fan-deltas were also scoured by both landslide material and tsunami runup causing localized changes in topography, particularly on fan-deltas 1988 and 1985 (Bloom et al., 2017). However, maximum scour depths of up to 10 m occur in only extremely localized areas of these fans. In fact, other areas of the fan surfaces increased up to 10 m in elevation (Bloom et al., 2017). Thus, no significant change in gradient across the fan-delta surfaces was found. Vegetation was almost or completely uprooted on all of the fan-deltas, suggesting some movement of unconsolidated alluvium on the fan surfaces as well. A period of redeposition of both landslide and fan-delta material elsewhere on the subaerial fan surfaces likely occurred following any initial scouring (Bloom et al., 2017). For these reasons, we assume that most of the sediment moved during the event was redistributed to other portions of the fan-delta surfaces with some loss of material to the fjord.

4.4.1 Fan-Delta 1988

The effects of the tsunamigenic landslide on the fan-deltas decreased with increased distance from the source at the head of the fjord. Thus, we believe the maximum possible error in volume estimates attributable to the event would be observed on fan-delta 1988. Fan-delta 1988 is located directly opposite the landslide and was the location of the highest recorded runup (192 m). To quantify the maximum effect the tsunami could have had on our final volume estimate for fan-delta 1988, we hypothetically assumed that 10 vertical meters of sediment was completely removed from its surface during the event and re-ran our volume model with the updated surface. Had 10 vertical meters of sediment been removed across the entire fan-delta surface, our volume estimate could be underestimated by ~13%. This translates to a missing volume of ~4 million m³ from our original estimate of 34.8 ± 3.8 million m³. In reality, a loss of up to 10 vertical meters was only observed in extremely localized areas on fan-delta 1988, not across the entire surface (Bloom et al., 2017). Therefore, this underestimate is considered extremely conservative.

The fan-deltas of Taan Fjord have been prograding for decades into Taan Fjord and any impacts from the 2016 landslide and tsunami were surficial. A previous study on the fan-deltas post-tsunami (Bloom et al., 2017) found that the primary changes that occurred on the fan-deltas were the removal of vegetation and redistribution of fan-delta sediment. This doesn't have a great impact on the total sediment package contained within the fan-deltas, and so we believe that the effects of the landslide and tsunami on volume estimations were minimal. At the realm of extreme possibility, volumes could have been underestimated by ~13% for those fans most affected, but it is likely to be much less than this figure.

4.5 Tyndall Glacier, Taan Tributaries, and the 2015 Landslide

The processes of paraglacial relaxation are varied in Taan Fjord but they are all demonstrably rapid, and the tributary watersheds are greater contributors of sediment to the fjord than Tyndall Glacier during its retreat. As previously mentioned, the combined volume of sediment stored in the fan-deltas of Taan Fjord in 2014 (pre-tsunami) was 165.7 ± 16.0 million m^3 . As of 1999, the total volume of sediment accumulated in the fjord from Tyndall Glacier was 56 million m^3 (Koppes and Hallet, 2006). Tyndall Glacier's 1962-1999 average sediment flux was 1.3 ± 0.2 million m^3yr^{-1} (Koppes and Hallet, 2006). Hence, the total projected volume of sediment that should have been contributed to the fjord by the glacier between 1962 and 2016 using this flux estimate was 78.1 ± 13.9 million m^3 . Based on projected errors for both the glacier and tributaries, the tributary valleys have contributed significantly more sediment to the fjord than Tyndall Glacier has contributed during its retreat (figure 4-4). Additionally, our volume estimates are considered minimum estimates as they only account for sediment accumulated in the fan-delta deposits and not the finer sediments that bypass the fan-delta altogether.

On average, the tributary valleys yielded 4.3 ± 0.3 million m^3 of sediment annually, which was over 3 times more than the glacier (1.3 ± 0.2 million m^3yr^{-1} , Koppes and Hallet, 2006). The landslide had an instantaneous yield that far exceeded that of both the glacier and tributary valleys at 76 million m^3 (Haeussler et al., in press). The instantaneous erosion rate for the landslide averaged over the area of the landslide scarp was also the highest with over 61 vertical meters of rock sliding into the fjord in mere seconds. The tributary valleys had a smaller average basin-averaged erosion rate of 36.0 ± 5.7 mm yr^{-1} . This was not significantly greater

than the average erosion rate of Tyndall Glacier between 1962 and 1999, which was $28 \pm 5 \text{ mm yr}^{-1}$ (Koppes and Hallet, 2006).

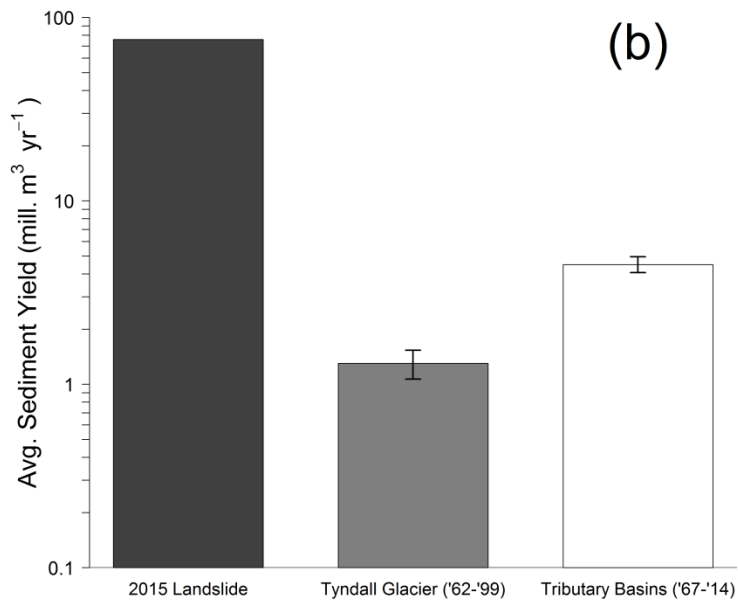
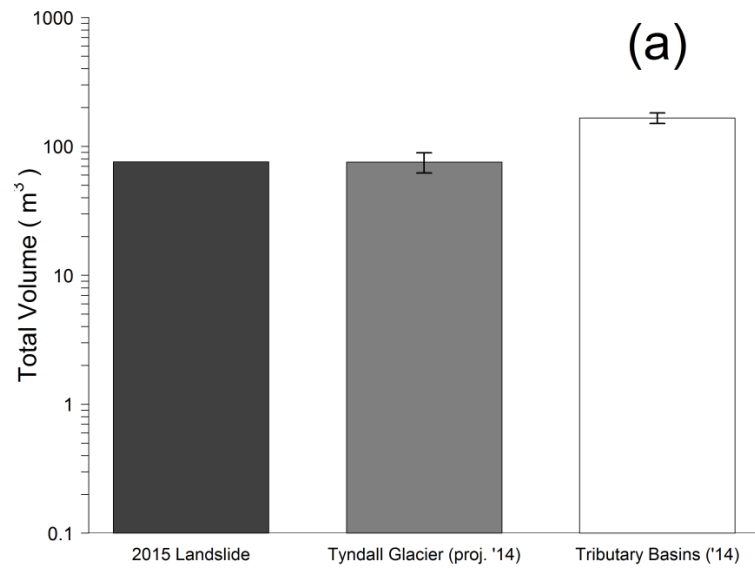
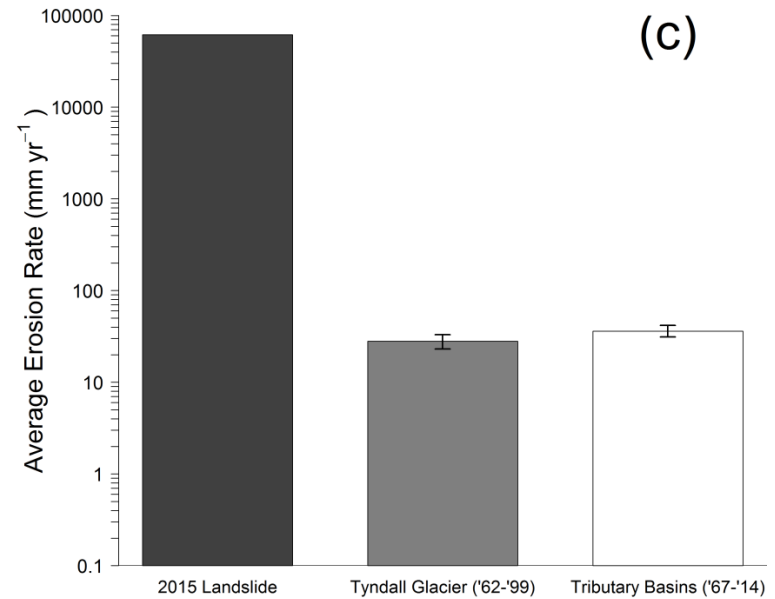


Figure 4-4. Graphs comparing the sediment output from the tributary watersheds to the sediment output of the glacier and the instantaneous output from the October 2015 landslide all on logarithmic scales. In **(a)**, total sediment volumes from the landslide (76 mill. m³), glacier (78.1 ± 13.9 mill. m³), and tributary basins (165.7 ± 16.0 mill. m³) are displayed. In **(b)**, the instantaneous yield for the landslide (76 mill. m³) is compared with the known yield from Tyndall Glacier (1.3 ± 0.2 mill. m³yr⁻¹) and the tributary basins (4.3 ± 0.3 mill. m³yr⁻¹). In **(c)**, the instantaneous erosion rate of the landslide (61.6 m), erosion rate of the glacier (28 ± 5 mm yr⁻¹), and combined average erosion rate of the tributary basins (36.0 ± 5.7 mm yr⁻¹) are displayed. Volume for Tyndall Glacier was projected from sediment flux data published in Koppes and Hallet, 2006. Their yield and erosion rate data were also used for the glacier in **(b)** and **(c)**. Volume of the landslide was obtained from Haeussler et al., 2017.



Our findings suggest that the tributary basins of Taan Fjord were on average as erosive and contributed more sediment to the fjord than Tyndall Glacier. This result was particularly impressive, as tidewater glaciers are known for being exceptionally erosive during phases of retreat (Hallet et al., 1996; Koppes and Hallet, 2002). Increased calving at the terminus of tidewater glaciers increases ice velocities, which in turn leads to enhanced delivery of ice to the calving front (Meier and Post, 1987; O'Neel et al., 2005; Vieli et al., 2015). With the delivery of more ice in this positive feedback loop comes an increase in the sediment flux from the glacier (Koppes and Hallet, 2002). Alaskan tidewater glaciers in particular yield high volumes of sediment during phases of retreat and have been found to have erosion rates that are orders of magnitude larger than anywhere else in the world (Hallet et al., 1996; Koppes and Hallet, 2002). With all of that in mind, we've been able to demonstrate that in fact, paraglacial basins can yield more sediment than these tidewater glaciers over decadal timescales following the onset of retreat.

Research on regions experiencing rapid deglaciation often focuses on the retreating glacier and the effects of its retreat on its sediment yield and erosive capabilities. Oftentimes, there is little consideration of other processes actively happening in the deglaciating environment at a land system scale, with the exception of a few recent studies (Knight and Harrison, 2014; Lane and Bakker, 2017). Our results show that where large tributary basins exist in a landscape experiencing rapid deglaciation, paraglacial processes can dramatically alter the landscape and at a faster rate than the local retreating glacier. Thus, their contribution to sediment yield estimates should not be ignored nor minimized.

4.6 Future Paraglacial Relaxation of Taan Fjord

The tributary basins of Taan Fjord will continue to undergo paraglacial relaxation until a new, post-glacial equilibrium is reached, barring any re-advance of Tyndall Glacier. The term “equilibrium” is often used to describe a river with a smooth, concave-up longitudinal profile (Rãdoane et al., 2003). However, the tributary basins in Taan Fjord don’t need to achieve this idealized shape in order to reach an equilibrium following retreat-induced base-level fall. We believe a more realistic indicator of paraglacial relaxation from the retreat of Tyndall Glacier in the tributaries would be the full migration of any knickpoints upstream or when the knickpoints are completely eroded away. The knickpoints were the main feature introduced into the tributary streams following glacier retreat and are thus a good indicator of the stage of relaxation in each tributary. The disappearance of the knickpoint would indicate the watershed is in a stage of relaxation on the waning side of the theoretical paraglacial relaxation curve where most paraglacially-derived sediment has been exhausted (red circle, figure 4-5).

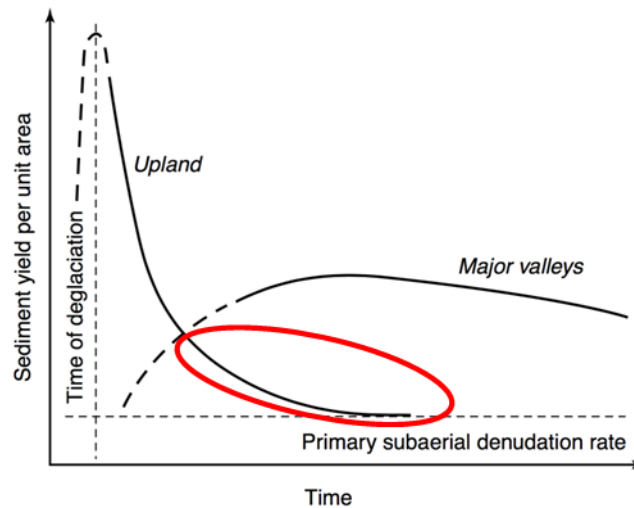


Figure 4-5. Relative sediment yield rates displayed as a comparison between small and major valleys (Ballantyne 2002; Church and Slaymaker, 1989). After complete knickpoint removal, we believe the tributary basins will have a sediment yield comparable to the curve within the red circle.

An example of a watershed we believe to have responded almost completely to base-level fall is watershed 1967. The knickpoint visible at the outlet of the stream in 1969 was completely removed by the river by 2016 (figure 3-5). The rate of change in this tributary is also observed in its sediment yield and basin-averaged erosion rate through time (figure 3-8, 3-10). Sediment accumulation was rapid and dynamic for a little over a decade at the onset of fan-delta formation, whereas in the decade prior to the 2015 tsunami, there appeared to be a tapering off in sediment accumulation. For this watershed, we therefore believe the paraglacial “peak” in sediment yield has already occurred. Had the tsunamigenic landslide not occurred and reorganized the subaerial surface, we believe sediment yield from this tributary would have continued to decline or remain relatively low.

In contrast, the watersheds at the head of the fjord are still undergoing dynamic change caused by their relative “youngness” (experienced base-level fall most recently) and active thrust faulting within their boundaries. The presence of knickpoints in watersheds 1985 and 1988, as well as the jump in sediment yields and erosion rates in watershed 1985 and 1987 between 2006 and 2014, all suggest they are in an earlier stage of paraglacial relaxation than those watersheds at the entrance of the fjord. Thus, paraglacial relaxation in Taan Fjord at the watershed scale is a function of the time since initial disturbance (base-level fall) and the lithology and structure of the bedrock in the watershed.

The 2015 tsunami almost completely stripped the fan-delta surfaces of all vegetation, therefore potentially reactivating previously stabilized portions of their surfaces. Some of the fan-deltas also lost several meters of sediment on their surfaces thereby altering the gradient at their channel mouths (Bloom et al., 2017). These effects will likely temporarily increase sediment yield until stabilizing vegetation can reestablish on the fan surfaces. Additionally, the

fan-deltas will likely rapidly prograde in response to dissection of their subaerial fronts and failures of some of their submarine surfaces (Bloom et al., 2017).

4.6.1 Timeline of Relaxation

Tyndall Glacier actively occupies the fjord and has advanced over landslide debris since 2015 (Bloom et al., 2017; Dufresne et al., 2018; Haeussler et al., in press). This makes any quantitative estimate of complete relaxation of the larger Taan Fjord/Tyndall Glacier speculative and likely spurious. The behavior of Tyndall Glacier will drive changes in the paraglacial landscape for decades to come. Given the high elevation of Tyndall Glacier's headwaters on the south face of Mount St. Elias, complete deglaciation in this catchment is unlikely, however it also remains uncertain how the glacier will respond in the future to climate change. If this recent advance is temporary and the glacier follows the global trend of terminus retreat in the future, the rate and amount retreat will dictate how fast new watershed outlets are exposed and thus the pace at which the landscape will change during deglaciation. Regardless of the future extent of Tyndall Glacier, paraglacial processes are likely to continue in the region for decades to centuries as climate continues to warm.

For large-scale paraglacial landscapes, such as catchments hundreds of square kilometers in size, large paraglacial alluvial fans can experience rapid growth for decades or centuries following deglaciation (Ryder, 1971). However, the tributary catchments in Taan Fjord are small in size and respond much quicker to disturbance than extremely large basins would. The watersheds in Taan Fjord that have had the most time to respond following the retreat of Tyndall Glacier (watersheds 1967, 1973, 1980, 1983, and 1984) have likely already experienced their peak paraglacial sediment yields. It is unclear whether watersheds 1985, 1987 and 1988 have reached their peak sediment yields, but recent heightened yields and very high erosion rates

suggest they have not. Thus, the scale-dependent qualification of landscapes as “paraglacial” remains of great importance when considering the timing of paraglacial relaxation. While small-scale relaxation has already peaked in some watershed systems in Taan Fjord, the paraglacial period for the larger scale Taan Fjord/Tyndall Glacier land system has only just begun.

Chapter 5: Conclusions

The paraglacial relaxation of Taan Fjord has been extreme in both “small-scale” unravelling of the landscape and the large-scale stochastic landslide event of 2015. We hesitate to use the phrase “small-scale” when referring to the paraglacial processes acting in the tributary basins because the sediment excavated from these watersheds exceeds that of the retreating tidewater glacier that occupies the fjord. While the landslide event mobilized a massive amount of sediment at the head of the fjord, it was the processes active in the tributary basins that have led to significant changes over a greater area. As the landscape began to relax following the onset of Tyndall Glacier’s retreat, these paraglacial processes have been exceedingly effective in altering the face of Taan Fjord.

The main findings of this study as they pertain to the study goals outlined in the introduction were as follows:

1. Tyndall Glacier has retreated a total of 17.25 km since 1961 (Koppes and Hallet, 2006) and thinned rapidly. In some cases, the thinning rate exceeded 20 m yr^{-1} . For the tributary basins of Taan Fjord, this resulted in an average base-level fall of $\sim 400 \text{ m}$ at the entrance to the fjord and over 500 m at the head of the fjord.
2. The tributary streams have responded to the retreat-induced base-level fall by incising into their lower reaches, thereby triggering the formation of rapidly migrating knickpoints. Additionally, the streams transitioned from braided to single-thread morphologies as a result of steepened channel gradients in their lower reaches.
3. In total, $165.7 \pm 16.0 \text{ m}^3$ of sediment has accumulated in the fan-deltas of Taan Fjord.
4. At the onset of fan-delta progradation, sediment yields and erosion rates in all the tributary basins were high and dynamic. Sediment yields and erosion rates tended to taper

off for those tributary basins exposed for the longest amount of time. This suggests that the basins at the entrance of the fjord have relaxed more than those at the head of the fjord.

5. The total volume of sediment contributed to Taan Fjord by the tributary basins since 1962 was double the amount contributed by Tyndall Glacier. The average annual sediment yield from the tributary basins is also three times more than that of Tyndall Glacier, however the annual basin-averaged erosion rates of Tyndall Glacier and the tributaries was found not to be significantly different. Over a few seconds, the 2015 landslide contributed a volume of sediment roughly equivalent to what the glacier has contributed since 1962.

5.1 General Conclusions

The rate at which the tributary basins have been eroding their watersheds and contributing sediment to their fan-deltas is primarily a function of these three variables: (1) the availability of non-cohesive sediment in the watershed, (2) the length of time since the watershed outlet experienced a sharp drop in base-level, and (3) the lithology and structure of the bedrock in the watershed.

Basins with large stores of loose sediment in the form of ice-marginal lake-bottom outwash and/or till deposits from Tyndall Glacier tended to have the highest yields at the beginning phase of fan-delta formation. This indicated that these paraglacial deposits were effectively flushed from the tributary systems immediately following the retreat of glacier ice past their outlets. Those basins with little to no paraglacial sediment storage have seen much smaller yields, suggesting the dominance of slow bedrock erosion in these watersheds. The structure of the bedrock within the basins also tended to enhance yields and erosion rates where

thrust faulting was active. This was seen exclusively in watersheds along the Chaix-Hills thrust fault at the head of the fjord. Surprisingly, the size of the contributing basin area seemed to have little effect on the rate at which sediment was evacuated from the basins with some of the smallest basins being the most erosive.

In terms of volume of sediment excavated from the watersheds and added to the fjord, the tributary basins have supplied the most. The amount of sediment that has been deposited on the tributary fan-deltas has been shown to be over two times more than the total volume contributed by Tyndall Glacier. This tributary-sourced sediment package was even greater than the instantaneous yield from the 2015 landslide.

This finding is significant because retreating Alaskan tidewater glaciers have been known to have sediment flux rates that are an order of magnitude larger than glaciers elsewhere (Hallet et al., 1996; Koppes and Hallet, 2002). This suggests that not only are retreating Alaskan tidewater glaciers particularly erosive, but the landscapes left behind in their wake can be even more so in the decades that follow retreat. Our results place emphasis on the need to account for very high sediment yields coming from highly dynamic tributary basins when studying landscapes experiencing rapid glacier retreat.

The remoteness of Taan Fjord meant that the effects of the ongoing paraglacial relaxation of the landscape didn't have any adverse effects on populations or infrastructure. Despite this, Taan Fjord can be held as an example of the potential processes and changes that could occur in other, more populated regions of the world experiencing rapid glacier retreat. As an example, communities living downstream of dams in glaciated landscapes may face future problems related to the infilling of reservoirs if upstream rivers exhibit behavior similar to the streams of Taan Fjord. Increases in sediment yield have also been known to change the course of rivers

and/or result in more frequent and severe flooding events, thereby threatening lives and infrastructure in downstream communities. Perhaps most alarming is the increased likelihood of large paraglacial events like the tsunamigenic Taan Fjord landslide happening in other areas of the world where fast-paced glacial retreat and debuttreasing of steep, glacier-carved slopes is becoming the norm. These events could potentially lead to significant loss of life and property, particularly where large bedrock masses have the potential to slide into large bodies of water such as the ocean or reservoirs.

The evolution the landscape of Taan Fjord has provided an excellent illustration of the short-term consequences of rapid glacier retreat. Like Tyndall Glacier, most glaciers on Earth will continue to retreat as climate continues to warm. Regardless of the rapidity of retreat, new paraglacial landscapes will certainly continue to be exposed. Our observations from Taan Fjord will therefore be useful in understanding the geomorphic processes likely to accompany rapid deglaciation in other parts of the world. Lessons learned in this study could serve to aid populations in glaciated regions in their preparation for a warmer era without the presence of large glaciers.

References

- Agisoft, L.L.C., 2014. Agisoft PhotoScan user manual: professional edition.
- Arsenault, A.M. and Meigs, A.J., 2005. Contribution of deep-seated bedrock landslides to erosion of a glaciated basin in southern Alaska. *Earth Surface Processes and Landforms*, 30(9), pp.1111-1125.
- Ballantyne, C.K. and Stone, J.O., 2013. Timing and periodicity of paraglacial rock-slope failures in the Scottish Highlands. *Geomorphology*, 186, pp.150-161.
- Ballantyne, C.K., 2002. Paraglacial geomorphology. *Quaternary Science Reviews*, 21(18), pp.1935-2017.
- Berthier, E., Schiefer, E., Clarke, G.K., Menounos, B. and Rémy, F., 2010. Contribution of Alaskan glaciers to sea-level rise derived from satellite imagery. *Nature Geoscience*, 3(2), pp.92-95.
- Bloom, C.K. 2017, 'Catastrophic landscape modification from massive landslide tsunamis; An example from Taan Fiord, Alaska', Master of Science in Geological Science, Central Washington University, Ellensburg WA.
- Blum, M.D. and Törnqvist, T.E., 2000. Fluvial responses to climate and sea-level change: a review and look forward. *Sedimentology*, 47(s1), pp.2-48.
- Bornhold, B.D., Harper, J.R., McLaren, D. and Thomson, R.E., 2007. Destruction of the first nations village of Kwalate by a rock avalanche-generated tsunami. *Atmosphere-ocean*, 45(2), pp.123-128.
- Bruhn, R.L., Pavlis, T.L., Plafker, G. and Serpa, L., 2004. Deformation during terrane accretion in the Saint Elias orogen, Alaska. *Geological Society of America Bulletin*, 116(7-8), pp.771-787.
- Brush, L.M. and Wolman, M.G., 1960. Knickpoint behavior in noncohesive material: a laboratory study. *Geological Society of America Bulletin*, 71(1), pp.59-74.
- Chapman, J.B., Pavlis, T.L., Bruhn, R.L., Worthington, L.L., Gulick, S.P. and Berger, A.L., 2012. Structural relationships in the eastern syntaxis of the St. Elias orogen, Alaska. *Geosphere*, 8(1), pp.105-126.
- Church, M. and Ryder, J.M., 1972. Paraglacial sedimentation: a consideration of fluvial processes conditioned by glaciation. *Geological Society of America Bulletin*, 83(10), pp.3059-3072.
- Chapman, J.B., Worthington, L.L., Pavlis, T.L., Bruhn, R.L. and Gulick, S.P., 2011. The Suckling Hills fault, Kayak Island zone, and accretion of the Yakutat microplate, Alaska. *Tectonics*, 30(6).
- Church, M. and Ryder, J.M., 1972. Paraglacial sedimentation: a consideration of fluvial processes conditioned by glaciation. *Geological Society of America Bulletin*, 83(10), pp.3059-3072.
- Church, M. and Slaymaker, O., 1989. Disequilibrium of Holocene sediment yield in glaciated British Columbia. *Nature*, 337(6206), pp.452-454.

- Church, M., 2015. Channel stability: morphodynamics and the morphology of rivers. In *Rivers—Physical, Fluvial and Environmental Processes* (pp. 281-321). Springer, Cham.
- Curran, J.H., Loso, M.G. and Williams, H.B., 2017. Glacial conditioning of stream position and flooding in the braid plain of the Exit Glacier foreland, Alaska. *Geomorphology*, 293, pp.272-288.
- Enkelmann, E., Zeitler, P.K., Pavlis, T.L., Garver, J.I. and Ridgway, K.D., 2009. Intense localized rock uplift and erosion in the St Elias orogen of Alaska. *Nature Geoscience*, 2(5), pp.360-363.
- Dadson, S.J., Hovius, N., Chen, H., Dade, W.B., Hsieh, M.L., Willett, S.D., Hu, J.C., Horng, M.J., Chen, M.C., Stark, C.P. and Lague, D., 2003. Links between erosion, runoff variability and seismicity in the Taiwan orogen. *Nature*, 426(6967), p.648.
- Dufresne, A., Geertsema, M., Shugar, D.H., Koppes, M., Higman, B., Haeussler, P.J., Stark, C., Venditti, J.G., Bonno, D., Larsen, C. and Gulick, S.P.S., 2018. Sedimentology and geomorphology of a large tsunamigenic landslide, Taan Fiord, Alaska. *Sedimentary Geology*, 364, pp.302-318.
- Elliott, J., Freymueller, J.T. and Larsen, C.F., 2013. Active tectonics of the St. Elias orogen, Alaska, observed with GPS measurements. *Journal of Geophysical Research: Solid Earth*, 118(10), pp.5625-5642.
- Enkelmann, E., Zeitler, P.K., Pavlis, T.L., Garver, J.I. and Ridgway, K.D., 2009. Intense localized rock uplift and erosion in the St Elias orogen of Alaska. *Nature Geoscience*, 2(5), pp.360-363.
- Eyles, N. and Kocsis, S.P., 1989. Reply to M. Church and JM Ryder's discussion of "sedimentology and clast fabrics of subaerial debris flow facies in glacially-influenced alluvial fan". *Sedimentary Geology*, 65(1), pp.197-198.
- Fischer, L., Purves, R., Huggel, C., Noetzi, J. & Haeberli, W., 2012. On the influence of topographic, geological and cryospheric factors on rock avalanches and rockfalls in high-mountain areas. *Natural Hazards and Earth System Sciences*, 12(1), pp. 241-254.
- Fonstad, M.A., Dietrich, J.T., Courville, B.C., Jensen, J.L. and Carbonneau, P.E., 2013. Topographic structure from motion: a new development in photogrammetric measurement. *Earth Surface Processes and Landforms*, 38(4), pp.421-430.
- Gilbert, R., 1975. Sedimentation in Lillooet Lake, British Columbia. *Canadian Journal of Earth Sciences*, 12(10), pp.1697-1711.
- Giles, P.T., 2010. Investigating the use of alluvial fan volume to represent fan size in morphometric studies. *Geomorphology*, 121(3), pp.317-328.
- Haeussler, P.J., Gulick, S.P.S., McCall, N., Walton, M., Reece, R., Larsen, C., Shugar, D.H., Geertsema, M., Venditti, J.G., Labay, K., (In press). Submarine deposition of a subaerial landslide in Taan Fiord, Alaska. *Journal of Geophysical Research*.
- Hallet, B., Hunter, L. and Bogen, J., 1996. Rates of erosion and sediment evacuation by glaciers: A review of field data and their implications. *Global and Planetary Change*, 12(1-4), pp.213-235.
- Hewitt, K., Clague, J.J. and Orwin, J.F., 2008. Legacies of catastrophic rock slope failures in mountain landscapes. *Earth-Science Reviews*, 87(1-2), pp.1-38.

- Hickin, E.J., 1989. Contemporary Squamish River sediment flux to Howe Sound, British Columbia. *Canadian Journal of Earth Sciences*, 26(10), pp.1953-1963.
- Higman, B., Shugar, D.H., Stark, C., Ekstrom, G., Koppes, M., Lynett, P., Dufresne, A., Haeussler, P.J., Geertsema, M., Gulick, S., Mattox, A., Vendditti, J.G., Walton, M.A.L., McCall, N., et al. (In press). An Alaskan landslide and tsunami induced by glacial retreat.
- Holbrook, J., Scott, R.W. and Oboh-Ikuenobe, F.E., 2006. Base-level buffers and buttresses: a model for upstream versus downstream control on fluvial geometry and architecture within sequences. *Journal of Sedimentary Research*, 76(1), pp.162-174.
- Huggel, C., 2009. Recent extreme slope failures in glacial environments: effects of thermal perturbation. *Quaternary Science Reviews*, 28(11-12), pp.1119-1130.
- Huss, M., Bookhagen, B., Huggel, C., Jacobsen, D., Bradley, R.S., Clague, J.J., Vuille, M., Buytaert, W., Cayan, D.R., Greenwood, G. and Mark, B.G., 2017. Toward mountains without permanent snow and ice. *Earth's Future*, 5(5), pp.418-435.
- Jaeger, J.M. and Koppes, M.N., 2016. The role of the cryosphere in source-to-sink systems. *Earth-Science Reviews*, 153, pp.43-76.
- Javernick, L., Brasington, J. and Caruso, B., 2014. Modeling the topography of shallow braided rivers using Structure-from-Motion photogrammetry. *Geomorphology*, 213, pp.166-182.
- Knight, J. and Harrison, S., 2014. Glacial and paraglacial environments. *Geografiska Annaler: Series A, Physical Geography*, 96(3), pp.241-244.
- Koppes, M. and Hallet, B., 2006. Erosion rates during rapid deglaciation in Icy Bay, Alaska. *Journal of Geophysical Research: Earth Surface*, 111(F2).
- Koppes, M., Sylwester, R., Rivera, A. and Hallet, B., 2010. Variations in sediment yield over the advance and retreat of a calving glacier, Laguna San Rafael, North Patagonian Icefield. *Quaternary Research*, 73(1), pp.84-95.
- Koppes, M.N. and Hallet, B., 2002. Influence of rapid glacial retreat on the rate of erosion by tidewater glaciers. *Geology*, 30(1), pp.47-50.
- Lane, S.N., Bakker, M., Gabbud, C., Micheletti, N. and Saugy, J.N., 2017. Sediment export, transient landscape response and catchment-scale connectivity following rapid climate warming and Alpine glacier recession. *Geomorphology*, 277, pp.210-227.
- Larsen, C.F., Motyka, R.J., Freymueller, J.T., Echelmeyer, K.A. and Ivins, E.R., 2005. Rapid viscoelastic uplift in southeast Alaska caused by post-Little Ice Age glacial retreat. *Earth and Planetary Science Letters*, 237(3), pp.548-560.
- Lastras, G., Amblas, D., Calafat, A.M., Canals, M., Frigola, J., Hermanns, R.L., Lafuerza, S., Longva, O., Micallef, A., Sepúlveda, S.A. and Vargas, G., 2013. Landslides cause tsunami waves: insights from Aysén fjord, Chile. *Eos, Transactions American Geophysical Union*, 94(34), pp.297-298.
- Leonard, E.M., 1997. The relationship between glacial activity and sediment production: evidence from a 4450-year varve record of neoglacial sedimentation in Hector Lake, Alberta, Canada. *Journal of Paleolimnology*, 17(3), pp.319-330.

- Mankhemthong, N., Doser, D.I. and Pavlis, T.L., 2013. Interpretation of gravity and magnetic data and development of two-dimensional cross-sectional models for the Border Ranges fault system, south-central Alaska. *Geosphere*, 9(2), pp.242-259.
- Marzeion, B., Cogley, J.G., Richter, K. and Parkes, D., 2014. Glaciers. Attribution of global glacier mass loss to anthropogenic and natural causes. *Science (New York, NY)*, 345(6199), pp.919-921.
- McColl, S.T., 2012. Paraglacial rock-slope stability. *Geomorphology*, 153, pp.1-16.
- Meier, M.F. and Post, A., 1987. Fast tidewater glaciers. *Journal of Geophysical Research: Solid Earth*, 92(B9), pp.9051-9058.
- Meigs, A., Krugh, W.C., Davis, K. and Bank, G., 2006. Ultra-rapid landscape response and sediment yield following glacier retreat, Icy Bay, southern Alaska. *Geomorphology*, 78(3), pp.207-221.
- Molnia, B.F., 2007. Late nineteenth to early twenty-first century behavior of Alaskan glaciers as indicators of changing regional climate. *Global and Planetary Change*, 56(1), pp.23-56.
- Nemec, W. and Steel, R.J., 1988. What is a fan delta and how do we recognize it. *Fan Deltas: sedimentology and tectonic settings*, pp.3-13.
- O'Neel, S., Pfeffer, W.T., Krimmel, R. and Meier, M., 2005. Evolving force balance at Columbia Glacier, Alaska, during its rapid retreat. *Journal of Geophysical Research: Earth Surface*, 110(F3).
- Owen, L.A. and Sharma, M.C., 1998. Rates and magnitudes of paraglacial fan formation in the Garhwal Himalaya: implications for landscape evolution. *Geomorphology*, 26(1-3), pp.171-184.
- Pachauri, R.K., Allen, M.R., Barros, V.R., Broome, J., Cramer, W., Christ, R., Church, J.A., Clarke, L., Dahe, Q., Dasgupta, P. and Dubash, N.K., 2014. *Climate change 2014: synthesis report. Contribution of Working Groups I, II and III to the fifth assessment report of the Intergovernmental Panel on Climate Change* (p. 151). IPCC.
- Perry, S.E., Garver, J.I. and Ridgway, K.D., 2009. Transport of the Yakutat terrane, southern Alaska: Evidence from sediment petrology and detrital zircon fission-track and U/Pb double dating. *The Journal of Geology*, 117(2), pp.156-173.
- Plafker, G., Moore, J.C., and Winkler, G.R., 1994. Geology of the southern Alaska margin. In *The Geology of Alaska* (pp. 389-448). Geological Society of America.
- Radić, V. and Hock, R., 2011. Regionally differentiated contribution of mountain glaciers and ice caps to future sea-level rise. *Nature Geoscience*, 4(2), p.91.
- Radić, V., Bliss, A., Beedlow, A.C., Hock, R., Miles, E. and Cogley, J.G., 2014. Regional and global projections of twenty-first century glacier mass changes in response to climate scenarios from global climate models. *Climate Dynamics*, 42(1-2), pp.37-58.
- Rădoane, M., Rădoane, N. and Dumitriu, D., 2003. Geomorphological evolution of longitudinal river profiles in the Carpathians. *Geomorphology*, 50(4), pp.293-306.
- Ryder, J.M., 1971. The stratigraphy and morphology of para-glacial alluvial fans in south-central British Columbia. *Canadian Journal of Earth Sciences*, 8(2), pp.279-298.
- Schaefli et al., 2007

- Saltus, R.W., Stanley, R.G., Haeussler, P.J., Jones III, J.V., Potter, C.J. and Lewis, K.A., 2016. Late Oligocene to present contractional structure in and around the Susitna basin, Alaska—Geophysical evidence and geological implications. *Geosphere*, 12(5), pp.1378-1390.
- Schaefli, B., Hingray, B. and Musy, A., 2007. Climate change and hydropower production in the Swiss Alps: quantification of potential impacts and related modelling uncertainties. *Hydrology and Earth System Sciences Discussions*, 11(3), pp.1191-1205.
- Schumm, S.A. and Rea, D.K., 1995. Sediment yield from disturbed earth systems. *Geology*, 23(5), pp.391-394.
- Schumm, S.A., 1993. River response to baselevel change: implications for sequence stratigraphy. *The Journal of Geology*, 101(2), pp.279-294.
- Slaymaker, O., 2009. Proglacial, periglacial or paraglacial?. Geological Society, London, Special Publications, 320(1), pp.71-84. Slaymaker, O., 2011. Criteria to distinguish between periglacial, proglacial and paraglacial environments. *Quaestiones Geographicae*, 30(1), pp.85-94.
- Slaymaker, O., 2011. Criteria to distinguish between periglacial, proglacial and paraglacial environments. *Quaestiones Geographicae*, 30(1), pp.85-94.
- Smith, M.W. and Vericat, D., 2015. From experimental plots to experimental landscapes: topography, erosion and deposition in sub-humid badlands from structure-from-motion photogrammetry. *Earth Surface Processes and Landforms*, 40(12), pp.1656-1671.
- Spotila, J.A., Buscher, J.T., Meigs, A.J. and Reiners, P.W., 2004. Long-term glacial erosion of active mountain belts: example of the Chugach–St. Elias Range, Alaska. *Geology*, 32(6), pp.501-504.
- Vanoni, V.A. ed., 2006, March. Sedimentation engineering. American Society of Civil Engineers.
- Verhoeven, G., 2011. Taking computer vision aloft—archaeological three-dimensional reconstructions from aerial photographs with photoscan. *Archaeological prospection*, 18(1), pp.67-73.
- Verhoeven, G., Doneus, M., Briese, C. and Vermeulen, F., 2012. Mapping by matching: a computer vision-based approach to fast and accurate georeferencing of archaeological aerial photographs. *Journal of Archaeological Science*, 39(7), pp.2060-2070.
- Vieli, A., 2015. Retreat instability of tidewater glaciers and marine ice sheets. *Snow and Ice-Related Hazards, Risks, and Disasters*, edited by: Haeberli, W., Whiteman, C., and Shroder, JF, Elsevier Science, Saint Louis, pp.677-712.
- Westoby, M.J., Brasington, J., Glasser, N.F., Hambrey, M.J. and Reynolds, J.M., 2012. ‘Structure-from-Motion’ photogrammetry: A low-cost, effective tool for geoscience applications. *Geomorphology*, 179, pp.300-314.
- Wieczorek, G.F., Geist, E.L., Motyka, R.J. and Jakob, M., 2007. Hazard assessment of the Tidal Inlet landslide and potential subsequent tsunami, Glacier Bay National Park, Alaska. *Landslides*, 4(3), pp.205-215.

Appendix I.: Structure from Motion Photogrammetry

A.1 Background

Structure from motion photogrammetry (SfM) is a method used to generate three-dimensional models of features or surfaces from a series of overlapping images (Agisoft, 2014). It has a wide variety of uses and has been employed by researchers spanning disciplines from archaeology to geomorphology (Fonstad et al., 2013; Javernick et al., 2014; Verhoeven, 2011; Verhoeven et al., 2012). It is typically used as a processing tool to generate high quality digital terrain models (DTMs) from unmanned aerial vehicle (UAV) surveys or other images taken in the field (Javernick et al., 2014). The quality of DTMs from SfM software rivals that of LiDAR at a fraction of the cost (Fonstad et al., 2013; Javernick et al., 2014).

Advancements in SfM software allow users to create DTMs of past landscapes using only historical imagery. Information regarding original camera positioning is also not needed, as new algorithms exclusively match features regardless of changes in scale or view point between images (Fonstad et al., 2013). This extends the potential for quantitative analyses decades into the past and opens up old datasets to new three-dimensional investigations.

This potential of SfM to produce high-quality models in years before high-resolution satellite imagery became available in addition to the abundance of aerial photographs taken of Taan Fjord made this method ideal to quantify changes in the fjord from 1957 to 1986. The DTM products produced with SfM were used to interpret changes along the surface of Tyndall Glacier as well as changes in the watersheds of the eight tributary basins.

A.2 Workflow

In total, four SfM DTMs were created for Taan Fjord using historical aerial imagery taken by the US Geological Survey (USGS) (table A-1). The DTMs were created using Agisoft

PhotoScan version 1.2.6, which will henceforth be referred to as Photoscan. A detailed workflow is described below and illustrated in figure A-1.

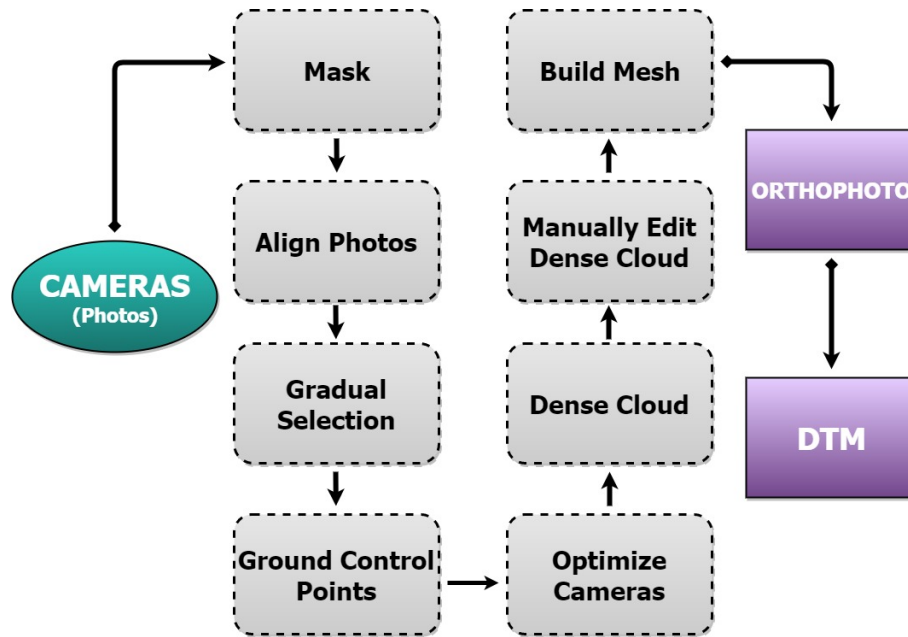


Figure A-1. Workflow of PhotoScan steps beginning with aerial photos and ending with a DTM.

The USGS photos were imported into Photoscan and those that contained borders and/or handwritten notes along the edges were masked out before alignment. If present, the water surface in the fjord was also masked to exclude icebergs which had the potential to move between successive photographs.

The photos were then aligned with medium accuracy and a sparse point cloud was generated from this initial alignment. There was little to no benefit in a higher accuracy during original alignment as it greatly increased processing time and resulted in lower-quality sparse point clouds. Once the sparse cloud was generated, the gradual selection tool was used to remove points that had reconstruction accuracies greater than 10 (poor accuracy) and reprojection errors greater than 1 or 2, depending on the model. These were the points that tended to lie far outside the sparse cloud and this automatic identification sped up the cleaning process. Points that remained far from the sparse cloud (if any) were then manually removed using the lasso tool.

Ground control points (GCPs) were added to the model before dense point cloud generation with the purpose of referencing the model to a known coordinate system (WGS 1984 Zone 7N). Others have documented the need for several highly accurate and well-spaced GCPs in order to create the highest accuracy model possible (Fonstad et al., 2012, Westoby et al., 2012). A low number of highly accurate, well-spaced GCPs will produce more accurate models than a high number of poorly placed GCPs (Smith et al., 2015). In this study, the number of GCPs varied per model, with the least being 5 and the most being 7.

Because historical aerial photos were being used, ground control points had to be manually placed. This was done by identifying immobile features in reference digital elevation models (DEMs) from June and August of 2016 (ArcticDEM). Features were deemed “immobile” if they persisted across all decades and appeared to have remained in place. Examples of GCPs that fit this definition included bedrock outcrops, boulders, persistent landforms, or distinctive patterns of vegetation. The GCPs for each model were created using ArcGIS and exported as text files into Photoscan. The software allows users to specify the coordinate system of the GCPs and they must be manually placed in the model with great care. Marker accuracy was therefore set to 2m to account for potential inexactness in GCP placement.

After setting GCPs, dense clouds were created using aggressive, high quality settings. Dense cloud generation is the most processing-intensive part of the process and took one to two hours on average to complete. Once generated, the model was inspected further and any suspect points were removed manually. Using the dense cloud as the input, a mesh was then created. A mesh is a complete surface composed of faces that is formed by connecting the points from the dense cloud. Finally, the mesh was used as an input to create an orthophoto.

Model	30 July 1957	25 August 1969	11 September 1973	12 September 1986
<i>Cameras</i>				
Camera Count	6	7	12	7
Flying Height(ft)	26,700	10,000	15,000	10,200
Image Type	BW	BW	BW	BW
<i>GCPs</i>				
Marker Count	7	6	6	5
Z GCP Error	0.90 m	3.58 m	2.86 m	2.96 m
Total XYZ GCP Error (m)	1.69 m	5.14 m	4.86 m	4.8 m
<i>Sparse Pt. Cloud</i>				
Point Count	19,872	113,567	221,118	154,370
Gradual Selection	Reconst. Uncertainty < 10 Reproj. Error < 1	Reconst. Uncertainty < 10 Reproj. Error < 2	Reconst. Uncertainty < 10 Reproj. Error < 1	Reconst. Uncertainty < 10 Reproj. Error < 1
Alignment Accuracy	Medium	Medium	Medium	Medium
Pair Preselection	Disabled	Disabled	Disabled	Disabled
<i>Dense Pt. Cloud</i>				
Point Count	33,738,417	51,037,172	109,269,766	63,532,914
Quality	High	High	High	High
Depth Filtering	Aggressive	Aggressive	Aggressive	Aggressive
<i>Model</i>				
Faces	2,999,999	2,284,935	3,000,000	3,000,000
Vertices	1,602,112	1,173,193	1,610,272	1,590,946
Surface Type	Height Field	Height Field	Height Field	Height Field
Source Data	Dense Cloud	Dense Cloud	Dense Cloud	Dense Cloud
Interpolation	Disabled	Disabled	Disabled	Disabled
Quality	High	High	High	High
<i>Orthoimage</i>				
Size (pix)	18,810 x 17,612	18,858 x 17,364	24254 x 41357	16914 x 22723
Blending Mode	Mosaic	Mosaic	Mosaic	Mosaic
Surface	Mesh	Mesh	Mesh	Mesh
Resolution (m)	1	0.379	0.5	0.384
Format (m)	tiff	tiff	tiff	tiff

Table A-1. Photoscan processing parameters.

The dense point cloud was exported as an LAS file and a DTM was created in ArcGIS using the LAS to Raster conversion tool in the Conversion toolbox. The DTM was not created in Photoscan as there was limited control over the interpolation technique used to generate a surface. Within the LAS Dataset to Raster tool, the interpolation method was set to “average,” which determines a value for one cell by finding the average value of all the points contained within that cell. Cell size was specified as 1 m x 1 m and the output was a 32-bit floating point raster.

A.3 Error Quantification

To determine model error, we compared each SfM DTM to a 2016 reference DTM (table 2-1). We identified the areas that likely remained the most “stable” since the aerial photographs were taken. Stable areas included bedrock outcrops that experienced little erosion and the fjord walls that have remained steep enough to restrict encroachment of vegetation. Areas that were bare in historical aerial photographs but vegetated in 2016 were avoided, as both DTMs are not bare-Earth products and the succession of vegetation could have resulted in larger than expected errors.

Once stable areas were identified, they were grouped into polygons and differenced from the 2016 DTM (figure A-2). If these polygons remained stable, there should have been little to no change in the surface elevation. Thus, we believe any difference found would provide a distribution of possible errors across the polygons. The mean value of the differenced DTM was taken as the average error in the model.

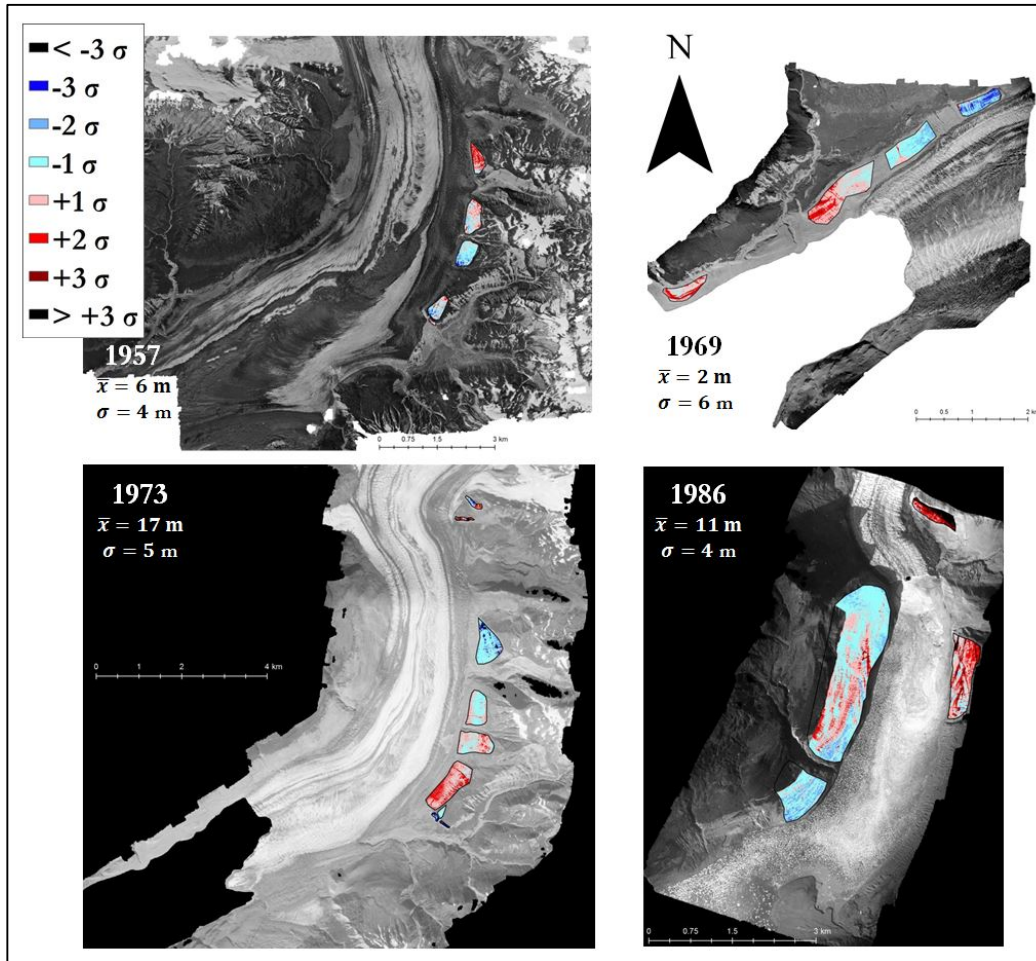


Figure A-2. The four models with associated error polygons. Positive errors are shaded red and negative errors are shaded blue.

It should be noted that Taan Fjord is an incredibly dynamic landscape and hence it was difficult to identify areas of “stability”. The fjord walls, for example, have undergone gullying since the retreat of Tyndall Glacier, but they were often the only relatively stable features present within the boundaries of both the SFM DTMs and the 2016 reference DTM. The estimates of model errors are therefore conservative (table A-2).

Model	1957	1969	1973	1986
Mean Error (m)	6	2	17	11
Standard Deviation (m)	4	6	5	4

Table A-2. Mean error and standard deviation of error distributions for each model.